Application of Duffing Method Integrating dq Transformation and Kurtosis in Bearing Fault Signal Detection

Haiyang Lou

School of Mechanical Engineering, Shijiazhuang Tiedao University, Shijiazhuang, 050000, Hebei, China; Department of Mechanical and Electrical Engineering, Hebei Vocational College of Rail Transportation, Shijiazhuang, 050000, Hebei, China. E-mail: 2202002006@student.stdu.edu.cn

Rujiang Hao

School of Mechanical Engineering, Shijiazhuang Tiedao University, Shijiazhuang, 050000, Hebei, China.

Qiang Xue

School of Electrical and Electronic Engineering, Shijiazhuang Tiedao University, Shijiazhuang, 050000, Hebei, China.

(Received 16 August 2025; accepted 25 October 2025)

Bearings in electric locomotives serve as core components of the transmission system. Their periodic impulsive fault signals are easily overwhelmed by intense noise, rendering traditional methods ineffective at extracting weak fault features under low signal-to-noise ratio (SNR) conditions, thereby limiting early diagnostic capabilities. To address this challenge, this paper proposes a bearing fault detection method that integrates the dq transformation, kurtosis statistics, and the Duffing chaotic oscillator: the dq transformation separates the periodic impulsive fault components, kurtosis statistics adaptively suppress noise, and the Duffing system identifies weak signal features. Comparative analyses using simulations and experiments demonstrate that the proposed method achieves higher fault detection accuracy in low-SNR environments, along with superior timeliness and stability in feature extraction.

1. INTRODUCTION

Rolling bearings, as core transmission components in rotating machinery, are widely employed in critical equipment such as electric locomotives and industrial motors.[1] Their health directly influences operational stability and reliability, and even impacts production safety and economic efficiency. Among bearing faults, those caused by localized defects are the most common, generating periodic impulsive signals with specific frequency characteristics. However, in real industrial settings, bearing vibration signals are often submerged in strong background noise from equipment operation and environmental interference. Particularly in early-stage faults, the impulsive signals exhibit low amplitude and energy, making effective separation of fault features from noise challenging. Traditional diagnostic approaches struggle to achieve accurate identification, severely constraining early fault detection in bearings.[2] Therefore, developing efficient methods for extracting weak periodic impulsive features under strong noise conditions holds significant theoretical value and engineering relevance.

To tackle the challenges in bearing fault feature extraction, researchers have conducted extensive studies. Traditional methods primarily rely on time-domain, frequency-domain, or time-frequency-domain analyses, such as time-domain statistical indicators, Fourier transforms, and wavelet transforms. However, these approaches depend heavily on manual feature selection, exhibit limited adaptability to non-stationary signals, and are prone to feature distortion in low-SNR environments.[3] In recent years, methods combining signal decomposition techniques with intelligent algorithms have gained widespread application, enabling the separation of fault components from complex signals. Nevertheless, issues such as mode mixing and parameter sensitivity persist, hindering precise capture of periodic impulsive features.[4] In the domain of weak-signal detection, the Duffing chaotic oscillator has emerged as an effective tool for signal extraction under strong noise, owing to its sensitivity to weak periodic signals and its robustness to noise. However, when used in isolation, it struggles with multi-component signal separation, and parameter settings strongly influence its noise tolerance.[5–11]

The dq transformation, a signal-processing technique based on coordinate rotation, has been successfully applied to motor fault diagnosis by decomposing complex multi-component signals into orthogonal d- and q-axis components to effectively separate fault-related features from interference.[12,13] Kurtosis, as a core indicator of signal non-Gaussianity, is highly sensitive to periodic impulsive signals and is commonly used for noise suppression and feature enhancement. However, in existing studies, kurtosis is often used as a fixed threshold, lacking adaptive integration with signal-processing workflows. Although the aforementioned techniques exhibit distinct advantages in their respective domains, no single method can comprehensively address the full pipeline of signal separation, noise suppression, and weak feature enhancement.

Based on the above analysis, this paper proposes a method for extracting weak fault features in bearings by integrating the dq transformation, kurtosis statistics, and the Duffing chaotic oscillator. The approach leverages the non-Gaussianity and periodicity of impulsive signals as core principles to construct a progressive processing framework: the dq transformation achieves separation of fault impulsive components from interference; kurtosis statistics adaptively adjust noise suppression parameters to enhance impulsive features while attenuating background noise; and the Duffing oscillator exploits its sensitivity to weak periodic signals for precise fault feature identification. The main innovations of this paper are as follows: (1) an adaptive fusion strategy for dq transformation and kurtosis statistics, optimizing signal separation by exploiting the non-Gaussian characteristics of periodic impulsive signals; (2) a comprehensive separation-suppression-enhancement processing framework for efficient extraction of weak impulsive features under strong noise; and (3) optimization of Duffing oscillator parameters tailored to bearing periodic impulsive signals, improving feature recognition robustness in low-SNR environments.

The paper is organized as follows: Section 2 presents the theoretical foundations of the Duffing oscillator; Section 3 elucidates the theoretical foundations of the dq transformation; Section 4 analyzes the theoretical aspects of the application of the Duffing method integrating dq transformation and kurtosis in bearing fault signal detection; Section 5 validates the method's effectiveness through simulation experiments and real data; and Section 6 concludes the paper and discusses future research directions.

2. CHARACTERISTICS ANALYSIS OF THE DUFFING SYSTEM

2.0.1. Dynamical Fundamentals of the Classical Duffing System

The classical Duffing system serves as a canonical model for describing nonlinear oscillations, with its dimensionless dynamical equation given by:[14–19]

$$\ddot{x} + \delta\dot{x} - \alpha x + \beta x^3 = \gamma u(t); \tag{1}$$

where: $\ddot{x}, \dot{x}, x$ represent the system state variables (normalized acceleration, velocity, and displacement, respectively); $\delta > 0$ denotes the damping coefficient, governing the energy dissipation rate and suppressing excessive expansion of chaotic regions; $\alpha < 0, \beta > 0$ are stiffness parameters that collectively establish a symmetric double-well potential topology (corresponding to the potential function $V(x) = \frac{\alpha}{2}x^2 + \frac{\beta}{4}x^4$); γ represents the excitation amplitude coefficient, modulating the energy proportion of the input signal; and $u(t)$ denotes the external excitation signal (vibration signals containing periodic impacts and noise in bearing fault detection).

To address the limitations of the classical Duffing system in bearing fault detection, such as high energy requirements for inter-well transitions, poor noise immunity, and lack of industrial adaptability,this paper analyzes a bistable Duffing system driven by constant excitation.

2.1. Mathematical Analysis of the Constant-Driven Duffing System

2.1.1. Mathematical Model and Physical Mechanism

Based on the Guckenheimer-Holmes global bifurcation theory and the requirement for stability in rolling bearing fault diagnosis, this paper adopts a bistable Duffing system driven by a d-axis constant bias. Its dimensionless dynamical model is strictly defined as:

$$\ddot{y} + \delta\dot{y} - \alpha y + \beta y^3 = C; \tag{2}$$

where: $y(t)$ is the system state variable (normalized displacement); $\delta > 0$ is the damping coefficient, which controls energy dissipation and suppresses expansion of chaotic regions; $\alpha < 0$, $\beta > 0$ construct a symmetric double potential well topology; and C is the equivalent d-axis constant drive.

The corresponding potential function is:

$$V(y) = \frac{\alpha}{2}y^2 + \frac{\beta}{4}y^4 - Cy. \tag{3}$$

The term $-Cy$ introduces a controllable tilt to the double potential well structure: when $C = 0$, the potential wells are fully symmetric, and inter-well motion requires overcoming the full potential barrier; when $C \neq 0$, the depth of one well increases while the other decreases, significantly reducing the excitation energy required for inter-well motion.

In the presence of weak periodic disturbances, impulses, or fault-induced perturbations, a moderate non-zero bias C enhances the coupling probability between potential wells, thereby producing stable large-amplitude inter-well responses or quasi-periodic trajectories. This mechanism does not rely on chaotic windows and provides: (1) Stable topology: attractor morphology remains consistent under small parameter perturbations, suitable for parameter fluctuations in industrial scenarios; (2) High sensitivity: the amplitude of inter-well response is positively correlated with the strength of weak fault perturbations, achieving fault signal amplification; and (3) Low excitation requirement: high-energy responses can be obtained solely through DC bias without large external periodic excitation.

Thus, the constant drive in this paper is not used to force the system into limit cycles but rather to enhance inter-well sensitivity via potential well tilting, enabling the Duffing system to function as a weak fault amplifier rather than a nonlinear oscillator, thereby balancing stability and sensitivity.

2.1.2. Feasibility of the Constant C

To simplify analysis and ensure reproducibility of results, standardized parameter settings are adopted: $\alpha = 1$, $\beta = 1$, under which the potential function simplifies to:

$$V(y) = -\frac{\alpha}{2}y^2 + \frac{\beta}{4}y^4 - Cy. \tag{4}$$

The extrema of the potential function satisfy the condition that its derivative is zero: $V'(y) = 0$. Substituting into Eq. (4) yields:

$$y^3 + y - C = 0. \tag{5}$$

The solution of this cubic equation determines the number and positions of equilibrium points, thereby reflecting the potential well structure (double well or single well).

For the cubic equation $y^3 + py + q = 0$ (here $p = 1$, $q = -C$), the discriminant is:

$$\Delta = -(4p^3 + 27q^2). \tag{6}$$

Substituting the parameters gives $\Delta = -4 - 27C^2$. The relationship between the sign of the discriminant, the number of real roots of the cubic equation, and the potential well structure is as follows: (1) When $\Delta < 0$, the cubic equation has three distinct real roots, corresponding to two local minima (potential well bottoms) and one local maximum (potential barrier top) in the potential function, i.e., a double potential well structure; (2) When $\Delta = 0$, the cubic equation has multiple roots (one minimum and one maximum merge); (3) When $\Delta > 0$, the cubic equation has only one real root, corresponding to one local minimum in the potential function, with the double potential well structure completely destroyed.

Setting $\Delta = 0$ yields the critical bias:

$$C_{\text{crit}} = \frac{2}{3\sqrt[3]{3}} \approx 0.38. \tag{7}$$

The physical and theoretical significance of this critical value is that the potential barrier height becomes zero if and only if $C > C_{\text{crit}}$, leaving the system with a single stable equilibrium point and completely destroying the double potential well structure, thereby inevitably resulting in a unique global attracting large-amplitude limit cycle across the wells.

3. PRINCIPLE OF DQ TRANSFORMATION

The conventional dq transformation (Park transformation) effectively decouples three-phase AC signals into DC quantities in a rotating frame, but its application requires complete three-phase input signals. To process single-channel bearing vibration signals, this paper employs a virtual two-phase dq transformation technique. Its core approach involves mathematically constructing an orthogonal virtual signal from the single-channel signal to form an α-β two-phase stationary coordinate system, followed by synchronous rotation transformation to extract components related to the fault characteristic frequency.

(1) Virtual two-phase construction

Let the acquired single-channel bearing vibration signal be $x(t)$. This paper uses the Hilbert transform to construct a strictly orthogonal virtual signal $\hat{x}(t)$, thereby forming the analytic signal:

$$z(t) = x(t) + j\hat{x}(t); \tag{8}$$

where $\hat{x}(t) = \mathcal{H}[x(t)] = \frac{1}{\pi}\text{P.V.}\int_{-\infty}^{\infty}\frac{x(\tau)}{t-\tau}d\tau$, and P.V. denotes the Cauchy principal value. The real and imaginary parts of the analytic signal $z(t)$ correspond to the components in the α-β stationary frame, i.e.:

$$x_\alpha(t) = x(t), \quad x_\beta(t) = \hat{x}(t). \tag{9}$$

This transformation is equivalent in the frequency domain to applying a -90° shift to all frequency components, ensuring that $x_\alpha(t)$ and $x_\beta(t)$ remain orthogonal at all frequencies with consistent amplitudes.

(2) Synchronous dq rotation transformation

The signals in the α-β frame are transformed into the dq frame rotating synchronously with the bearing fault characteristic angular frequency ω_f, using the transformation matrix:

$$\begin{bmatrix} x_d(t) \\ x_q(t) \end{bmatrix} = \begin{bmatrix} \cos(\omega_f t) & \sin(\omega_f t) \\ -\sin(\omega_f t) & \cos(\omega_f t) \end{bmatrix} \begin{bmatrix} x_\alpha(t) \\ x_\beta(t) \end{bmatrix}. \tag{10}$$

When the rotation frequency ω_f is precisely synchronized with the fundamental frequency of the periodic impulses in the signal, the impulsive components are converted into prominent slowly varying components in the d-axis signal $x_d(t)$, while noise and unrelated harmonics are effectively suppressed. The transformed d-axis signal can be approximated as:

$$x_d(t) \approx A_0 + \sum_k m_k h(t - t_k) + \tilde{n}(t); \tag{11}$$

where A_0 is the DC bias, $h(t - t_k)$ is the response to the k-th impulse, and $\tilde{n}(t)$ is the attenuated noise.

4. PHASE TRAJECTORY ANALYSIS OF THE BISTABLE DUFFING SYSTEM UNDER FOUR TYPES OF EXCITATION

4.1. Phase Trajectory Analysis under Pure Noise Excitation

Consider a bistable Duffing system driven by zero-mean Gaussian white noise:[20]

$$\ddot{y} + \delta\dot{y} - \alpha y + \beta y^3 = n_d(t); \tag{12}$$

where $\mathbb{E}[n_d(t)] = 0$ and $\mathbb{E}[n_d(t)n_d(\tau)] = 2D\delta(t - \tau)$ ($\delta(\cdot)$ is the Dirac delta function, distinct from the damping coefficient δ).

Since white noise is non-differentiable, Eq. (12) must be converted into a stochastic differential equation:

$$\begin{cases} \mathrm{d}y = \dot{y}\mathrm{d}t; \\ \mathrm{d}\dot{y} = (\alpha y - \beta y^3 - \delta\dot{y})\mathrm{d}t + \sqrt{2D}\mathrm{d}B(t); \end{cases} \tag{13}$$

where $B(t)$ is standard Brownian motion.

The probability density $p(y, \dot{y}, t)$ of the system state satisfies the Fokker-Planck-Kolmogorov (FPK) equation:

$$\frac{\partial p}{\partial t} = -\frac{\partial}{\partial \dot{y}}(\dot{y}p) - \frac{\partial}{\partial y}\left[(\alpha y - \beta y^3 - \delta\dot{y})p\right] + D\frac{\partial^2 p}{\partial y^2}. \tag{14}$$

In steady state, the stationary probability density is:

$$p(y, \dot{y}) = \frac{1}{Z}\exp\left(-\frac{\delta\dot{y}^2 + 2V(y)}{D}\right); \tag{15}$$

where: $p(y, \dot{y})$ is the stationary probability density of the state $(y, \dot{y})$; δ is the damping coefficient; $V(y)$ is the system potential function; D is the noise intensity; and Z is the normalization constant (essential for ensuring the validity of the probability density).

The normalization constant Z satisfies:

$$Z = \int_{-\infty}^{\infty}\int_{-\infty}^{\infty}\exp\left(-\frac{\delta\dot{y}^2 + 2V(y)}{D}\right)\mathrm{d}y\mathrm{d}\dot{y}. \tag{16}$$

Influence of noise intensity:

- Under weak noise ($D \ll \min V(y)$): The potential term $\frac{2V(y)}{D}$ dominates the exponential distribution, concentrating $p(y,\dot{y})$ at the bistable potential minima $y = \pm\sqrt{\frac{\alpha}{\beta}}$, confining the system within the wells.
- Under strong noise ($D \gg \max V(y)$): The potential term becomes negligible ($\frac{2V(y)}{D} \approx 0$), degenerating the probability density to $p(y,\dot{y}) = \frac{1}{Z'}\exp\left(-\frac{\delta\dot{y}^2}{D}\right)$, with a nearly uniform position distribution.

The distribution characteristics in phase space (y-$\dot{y}$ plane) directly reflect the stochastic dynamics. The differences under weak/strong noise are summarized in Table 1.

Table 1 summarizes the differences in phase diagrams of the bistable Duffing system under strong and weak noise excitation. Under weak noise ($D \ll \min V(y)$), the potential function term $\frac{2V(y)}{D}$ dominates the exponential distribution, confining phase points within the potential well; under strong noise ($D \gg \max V(y)$), the potential function term is negligible, and the phase point distribution is nearly uniform, reflecting the stochastic dynamic characteristics of the system under different noise intensities.

4.2. Constant Excitation $x_d(t) = A$

The governing equation of the bistable Duffing system is:

$$\ddot{y} + \delta\dot{y} - \alpha y + \beta y^3 = A. \tag{17}$$

The constant excitation tilts the bistable potential $V(y) = -\frac{\alpha}{2}y^2 + \frac{\beta}{4}y^4 - Ay$ from bistable to monostable, yielding a steady-state periodic orbit.

Proof of orbit existence: Construct the Lyapunov function $L(y,\dot{y}) = \frac{1}{2}\dot{y}^2 + V(y)$. Its time derivative is:

$$\dot{L} = \dot{y}\ddot{y} + \frac{\mathrm{d}V}{\mathrm{d}y}\dot{y} = -\delta\dot{y}^2 \le 0. \tag{18}$$

By LaSalle's invariance principle, trajectories converge to an invariant set.

Orbit analytic equation and geometric features: Multiplying both sides of Eq. (18) by $\dot{y}$ and integrating eliminates time, yielding the energy conservation form:

$$\frac{1}{2}\dot{y}^2 - \frac{\alpha}{2}y^2 + \frac{\beta}{4}y^4 - Ay = E_0. \tag{19}$$

Geometric morphology: Corresponds to quasi-elliptical convex closed trajectories, slightly flattened in the y-direction due to the nonlinear βy^4 term, symmetric and C^∞ smooth in the $\dot{y}$-direction.

4.3. Constant + Noise $x_d = A + n_d(t)$

The system response decomposes as $y = y_p(t) + \eta(t)$, where $y_p(t)$ is the limit cycle solution under constant excitation, and $\eta(t)$ is a zero-mean random perturbation.

Substituting $y(t)$ into the governing equation and using $\ddot{y}_p + \delta\dot{y}_p - \alpha y_p + \beta y_p^3 = A$, neglecting higher-order terms yields the linearized stochastic equation:

$$\ddot{\eta} + \delta\dot{\eta} + (3\beta y_p^2 - \alpha)\eta = n_d(t). \tag{20}$$

Let the time-varying effective stiffness be $k(t) = 3\beta y_p^2 - \alpha$ (periodic); then $\eta(t)$ is a zero-mean stationary random process with variance $\sigma_\eta^2 \propto \sigma_n^2 D$ (σ_n is the noise standard deviation and D is a damping-related coefficient).

Geometric morphology: Phase space exhibits a diffuse annular band centered on the limit cycle, with bandwidth proportional to σ_n.

Topological properties: The diffuse band is centrosymmetric, combining convergent periodic skeleton with noise-induced irregularity.

4.4. Constant + Noise + Periodic Impulses

The excitation form is:

$$x_d(t) = A + n_d(t) + \frac{A_k}{k_m}ke^{-\xi(t-t_k)}H(t-t_k). \tag{21}$$

The impulsive term is a decaying exponential pulse $H(t-t_k)$ is the Heaviside step function, $\xi > 0$ is the decay coefficient, T_{imp} is the impulse period), resulting in composite dynamics of limit cycle + noise diffusion + impulsive jumps.

(1) Dynamics at impulse instants

Since the impulse duration $\Delta t \ll T_{\text{imp}}$, damping and nonlinear terms are neglected. Integrating over the impulse interval yields the velocity increment:

$$\Delta\dot{y}\big|_{t_k} \approx \frac{A_k}{k_m\xi}. \tag{22}$$

The velocity increment is proportional to A_k and inversely proportional to ξ, causing instantaneous jumps along the $\dot{y}$-axis.

(2) Phase diagram features

Geometric morphology: The baseline trajectory is a diffuse band around a fixed ring (due to noise); superimposed periodic impulses introduce additional repetitive dense trajectory bundles at fixed intervals.

Topological properties: Impulses cause sudden state jumps (position/velocity), manifesting as sharp corners in otherwise smooth trajectories, with high density near corners.

The phase diagram characteristics under the four signal types are summarized in Table 2.

Table 2 summarizes the forms of d-axis components after dq transformation, phase trajectory characteristics of the Duffing system, and corresponding physical meanings under four typical excitations (pure noise, pure periodic signal, periodic signal + noise, fault impulses + noise). It corely reflects the synergy of "signal preprocessing (dq transformation) + nonlinear detection (Duffing system)": dq transformation achieves preliminary purification of fault features through spectral manipulation, and the Duffing system converts weak periodic impulse features into stable ring-peak coupling topological structures in phase space, providing a theoretical basis for fault detection in low signal-to-noise ratio (SNR) environments.

Theoretical analysis indicates that phase diagrams arise from the synergistic effect of signal preprocessing and nonlinear detection. The virtual dq transformation initially cleanses fault features via spectral operations. At the same time, the Duffing system acts as a feature amplifier, converting weak periodic impulsive characteristics into stable, explicit topological

Table 1. Characteristics of noise phase diagrams.

Characteristic Dimension	Strong Noise Behavior	Weak Noise Behavior
Distribution Morphology	Phase points diffuse uniformly across the entire phase space, with no distinct clustering regions	Phase points concentrate at potential minima $y = \pm\sqrt{\frac{\alpha}{\beta}}$
Topological Properties	Random large inter-well jumps, trajectories covering the full phase space	Local diffusion within wells rare inter-well jumps

Table 2. System response characteristics under typical excitations.

Excitation Type	d-Axis Component $x_d(t)$ (dq Transformed)	Duffing Phase Trajectory Characteristics	Physical Interpretation
Pure noise	Zero-mean stationary random process	Uniform phase point diffusion (no distinct attractor)	System baseline noise response
Pure periodic signal	Stable DC component A_0	Smooth, regular stable limit cycle	Fault-free steady-state operation
Periodic signal + noise	$A_0 + \tilde{n}(t)$	Diffuse band around limit cycle (bandwidth $\propto$ noise power)	Noise perturbation on deterministic signal
Fault impulses + noise	$A_0 + \sum_k m_k h(t - t_k) + \tilde{n}(t)$	Noise diffuse band + periodic "sharp-corner" inter-well jumps (local dense regions)	Qualitative fault signature (identifiable phase features)

features (a ring-peak coupling structure) in phase space. This paradigm shift from time-domain analysis to phase-space dynamical pattern recognition forms the theoretical foundation for the proposed method's high-robustness fault detection in low-SNR environments.

5. KURTOSIS-GUIDED ADAPTIVE MECHANISM

5.1. Gaussianity Detection Based on Kurtosis

Conventional Duffing oscillators employ fixed-amplitude periodic excitation, lacking adaptability to local noise characteristics. To address this limitation, a kurtosis-based gating mechanism is introduced.

Kurtosis is defined as the standardized fourth-order moment of a random variable Y:

$$K_F(Y) = \frac{\mu_4}{\mu_2^2} - 3; \tag{23}$$

where $\mu_2 = E[Y^2]$ and $\mu_4 = E[Y^4]$. For Gaussian processes, $K_F(Y) = 0$, and this property remains invariant under linear transformations, including bandpass filtering. Thus, kurtosis serves as an effective indicator of non-Gaussianity caused by structural or impulsive components.

A sliding-window estimation is adopted:

$$\hat{K}_F(t) = \frac{\frac{1}{N_w}\sum_{\tau\in W(t)}(Y(\tau) - \hat{\mu}(t))^4}{\left(\frac{1}{N_w}\sum_{\tau\in W(t)}(Y(\tau) - \hat{\mu}(t))^2\right)^2} - 3; \tag{24}$$

where $W(t)$ is the window centered at t, N_w is the window length, and $\hat{\mu}(t)$ is the sample mean. The variance of this estimator is approximately:

$$\mathrm{Var}(\hat{K}_F(t)) \approx \frac{24}{N_w}. \tag{25}$$

5.1.1. Weighting Function Design

The non-Gaussianity measure is defined as:

$$A(t) = |\hat{K}_F(t)|. \tag{26}$$

A smooth sigmoid gating function is then constructed:

$$W(t) = \frac{1}{1 + \exp[-s(A(t) - K_{thr})]}, \quad s > 0; \tag{27}$$

where s controls steepness, and K_{thr} is the threshold determined by significance level α:

$$K_{thr} = z_{\alpha/2} \cdot \sqrt{\frac{24}{N_w}}. \tag{28}$$

When $A(t)$ approaches zero, $W(t) \approx 0$; when $A(t)$ exceeds the threshold, $W(t) \approx 1$.

5.1.2. Embedded KG-Duffing System

The Duffing oscillator is improved by incorporating the gating function:

$$\ddot{x} + \mu\dot{x} + \alpha x + \beta x^3 = \gamma W(t)u(t); \tag{29}$$

where $u(t)$ is the input signal comprising weak target $r(t)$ and noise.

For Gaussian-dominated segments ($A(t) \approx 0$), excitation is suppressed, preventing pseudo-periodic trajectories. For signal-dominated segments ($A(t) \gg K_{thr}$), excitation is preserved, facilitating weak signal amplification. This adaptive gating mechanism balances sensitivity to weak targets with noise robustness, offering significant improvement over classical Duffing systems.

5.2. Design of Kurtosis-Weighted dq-Duffing System

This section aims to develop a novel Duffing detection system that integrates a kurtosis-guided mechanism. Kurtosis provides a critical criterion for distinguishing bearing fault impulses (high kurtosis, non-Gaussian) from background noise (low kurtosis, near-Gaussian). The core concept is to transform kurtosis from an offline evaluation metric into an online, adaptive system-control parameter, thereby enabling intelligent, selective response in the Duffing system.

5.2.1. System Architecture and Integration Principle

Based on the foregoing analysis, this paper designs a kurtosis-weighted dq-Duffing system (KWDS). Instead of directly using the preprocessed signal $x_d(t)$ as excitation, it is combined with real-time kurtosis information computed from the signal itself. The core dynamical equation is defined as:

$$\ddot{y} + \delta\dot{y} - \alpha y + \beta y^3 = \gamma \cdot [W(t) \cdot x_d(t)]; \tag{30}$$

with the adaptive weighting function driven by the real-time kurtosis estimator $\hat{K}_F(t)$:

$$W(t) = \frac{1}{1 + \exp[-s(\hat{K}_F(t) - K_{thr})]}. \tag{31}$$

The innovation of this design lies in closing the loop between the signal's intrinsic statistical property (kurtosis) and the nonlinear system's dynamical response (phase trajectory). The weighting function $W(t)$ acts as an intelligent gate, directly regulating the intensity or on/off state of the effective excitation $x_d(t)$ injected into the Duffing system.

5.2.2. Response Mechanism and Method Advantages

The superior performance of the system stems from its differential processing of different signal components:

1. Suppression of noise and pseudo-impulses: When a signal segment is dominated by random noise (corresponding to $\hat{K}_F(t) \to 0$), the weight $W(t) \approx 0$. Regardless of random pulses (pseudo-impulses) caused by noise in $x_d(t)$, the effective excitation intensity is greatly attenuated. This prevents the Duffing system from accumulating sufficient energy from non-periodic random disturbances, effectively suppressing pseudo-periodic trajectories and pseudo-impulse features, thereby reducing false alarms at the source.

2. Enhancement and preservation of true fault impulses: When a signal segment contains genuine periodic bearing fault impulses (corresponding to $\hat{K}_F(t) > K_{thr}$), the weight $W(t) \approx 1$. The effective excitation $x_d(t)$ containing true impulse features is injected into the Duffing system with almost no attenuation. The impulse energy fully drives the system, eliciting clear, stable "ring-peak coupling" phase trajectories. Thus, true fault features are not suppressed but highlighted against a cleaner background.

Traditional Duffing systems exhibit inherent high sensitivity to weak periodic or quasi-periodic disturbances, but this also renders them prone to noise interference. The proposed kurtosis-weighted Duffing system, through its kurtosis-guided intelligent gating, achieves a critical evolution in response mode:

1. Directed enhancement of response acuity: The system adaptively filters irregular pseudo-impulses with statistical properties similar to noise, responding selectively only to target excitations matching fault characteristics.

2. Precise reinforcement of core sensitivity: Sensitivity and discriminability are maintained or enhanced for true fault impulses exhibiting non-Gaussian impulsive features.

This leap from indiscriminate sensitivity to selective acuity constitutes the core mechanism enabling high-precision, low-false-alarm fault detection under strong noise. It ensures diagnostic responses only when genuine fault features are captured, significantly improving reliability and robustness.

5.3. Dynamical Improvement Analysis of Kurtosis Weighting Mechanism on Duffing System Chaotic Threshold

To quantitatively elucidate the advantages of the kurtosis-weighted mechanism in suppressing spurious noise-induced responses and enhancing the detection capability for weak periodic impacts from a nonlinear dynamics perspective, this section employs the Melnikov method and the Largest Lyapunov Exponent (LLE) for analysis.

Conventional Duffing systems are prone to spurious inter-well transitions under strong noise interference. The root cause lies in random, large-amplitude pulses within the noise that perturb the homoclinic orbit, leading to pseudo-chaotic or pseudo-periodic responses. The kurtosis-weighted mechanism proposed in this paper calculates a sliding-window kurtosis from the original vibration signal $x(t)$ to adaptively generate a gating function $W(t)$. This function permits the d-axis component $x_d(t)$, obtained via dq transformation, to serve as the effective excitation only when genuine non-Gaussian impacts are present. This design optimizes the system's dynamic response environment by selectively regulating the excitation components.

Consider a standardized symmetric bistable Duffing system:

$$\ddot{y} + \delta\dot{y} - \alpha y + \beta y^3 = \gamma \cdot p(t); \tag{32}$$

where $\mathbf{p}(t) = W(t) \cdot x_d(t)$ represents the effective excitation. $W(t)$ is computed based on the real-time kurtosis estimate of the original signal $x(t)$, and $x_d(t)$ is the low-frequency component derived from synchronous demodulation via the dq transformation, containing the transient characteristics of fault impacts and residual noise.

In the absence of perturbation, this system possesses a symmetric double-well potential. Its standard homoclinic orbit solution is given by:

$$q_0(t) = \sqrt{\frac{2\alpha}{\beta}}\text{sech}(\sqrt{\alpha}t) = \sqrt{2}\text{sech}(t). \tag{33}$$

The Melnikov function is utilized to measure the distance between the stable and unstable manifolds under small perturbations:[21–23]

$$M(t_0) = \int_{-\infty}^{\infty} \dot{q}_0(t)\left[-\delta\dot{q}_0(t) + \gamma p\left(t + t_0\right)\right] dt. \tag{34}$$

In the traditional system (where $W(t) \equiv 1$), the direct injection of raw noise causes random pulses to easily drive $M(t_0)$ across zero, inducing pseudo-homoclinic bifurcations and spurious inter-well transitions.

Within the kurtosis-weighted mechanism: (1) Gaussian-Noise-Dominant Segment: When the kurtosis of the original signal $\hat{K}_F(t) \approx 0$, it corresponds to $W(t) \approx 0$, resulting in $p(t) \approx 0$. Consequently, the noise disturbance is almost

entirely suppressed. (2) Genuine-Periodic-Impact Segment: When the kurtosis of the original signal increases significantly, corresponding to $W(t) \approx 1$, then $p(t) \approx x_d(t)$. The system excitation thus becomes the low-frequency component that aggregates the periodic impact information after demodulation.

The kurtosis-weighted mechanism attenuates the effective disturbance intensity of the noise, significantly raising the perturbation amplitude required for the $M(t_0)$ function to cross zero. This effectively suppresses spurious responses induced by noise. Simultaneously, because the periodic impact components in $x_d(t)$ have been concentrated into a purer low-frequency form via the dq transformation, the system's response sensitivity and reliability to genuine fault impacts are markedly enhanced within the high signal-to-noise ratio environment created by effective noise suppression.

6. EXPERIMENTAL VALIDATION AND ANALYSIS

This section systematically validates the effectiveness, robustness, and superiority of the proposed "Duffing system integrating dq transformation and kurtosis for detecting weak bearing faults under strong noise" using simulation signals and test-rig data. Comparisons are conducted against traditional Duffing and variational mode decomposition (VMD) methods across three dimensions: pseudo-suppression capability, true feature preservation, and comprehensive performance.

6.1. Simulation Analysis

This experiment aims to verify the detection performance of the Duffing system under synergistic dq transformation and kurtosis guidance for weak bearing faults. Core parameter configurations are listed in Table 3.

Table 3 presents the core parameter configuration for simulation experiments, covering simulation parameters (duration, sampling points, SNR), Duffing system parameters (damping, stiffness, excitation coefficient, etc.), kurtosis guidance parameters (threshold, window size, etc.), and fault signal parameters (characteristic frequency, resonance frequency, etc.). The parameter settings are based on the dynamic characteristics of the bistable Duffing system and the features of bearing fault signals, ensuring the repeatability and validity of experimental results, and laying a foundation for the comparative analysis of four subsequent experimental conditions (traditional Duffing + pure noise, kurtosis-weighted Duffing + pure noise, traditional Duffing + dq-transformed fault signal, kurtosis-weighted Duffing + dq-transformed fault signal).

Comparative phase trajectory analysis is conducted by evaluating four distinct conditions: (1) a conventional Duffing system under pure noise excitation without dq transformation or kurtosis weighting, (2) a kurtosis-weighted Duffing system under pure noise excitation without dq transformation, (3) a conventional Duffing system excited by the x_d fault component extracted via dq transformation but without kurtosis weighting, and (4) a kurtosis-weighted Duffing system excited by the dq-transformed x_d fault component.

The signal analysis and preprocessing process is illustrated in Fig. 1.

Figure 1 illustrates the signal preprocessing pipeline of the proposed method, which effectively extracts weak periodic fault-induced impulses in bearings from intense background noise. The figure comprises six subfigures arranged in the order of processing to reveal the internal mechanism of each step.

Observed Signal and Its Theoretical Model

Figure 1(a) Raw Fault Signal: The signal is dominated by high-intensity, broadband background noise, resulting in a cluttered waveform where the underlying periodic fault impulses are entirely submerged. This visually reflects the diagnostic challenge posed by the low signal-to-noise ratio (SNR ≈ -5 dB).

Figure 1(b) Pure Fault Impulses: This subfigure presents the theoretical model of the fault impulse component (solid curve). It consists of a series of decaying oscillatory pulses with a period of $T = 1/f_{\text{fault}} = 10$ ms, where the pulse interval strictly equals the fault characteristic period.

Feature Enhancement and Weighting

Figure 1(c) d-axis Signal $x_d(t)$: This is the d-axis component (dashed curve) obtained by applying a dq (Park) transformation synchronized with the fault characteristic frequency f_{fault} to the raw signal (a). Post-transformation, the fault frequency components are converted and accentuated as near-DC and low-frequency amplitude modulations, while high-frequency noise is suppressed.

Figure 1(d) Kurtosis Weighting Function $W(t)$: This is the frequency-domain weighting function (dotted pulse-like curve) calculated based on signal (c), with the horizontal axis representing time. Due to the high sensitivity of kurtosis to impulsive components, $W(t)$ exhibits prominent peaks at the fault characteristic frequency and its harmonics, while assigning low weights to noise-dominated frequency bands. This achieves automatic identification and enhancement of fault features in the frequency domain.

Figure 1(e) Pure Noise Signal: As a control group, this subfigure shows the time-domain waveform of pure Gaussian white noise (dash-dot curve) with energy equivalent to that in subfigure (a). Its waveform exhibits random characteristics without any periodic structure, serving to validate the method's robustness against noise.

Figure 1(f) verifies that the constructed weighting mechanism will not generate false responses to impulse-free interference by virtue of the characteristics of rapid weight attenuation, no significant fluctuations, and extremely low response under the input of impulse-free pure noise. Combined with the peak response characteristic of Fig. 1(d) to impulse-containing fault signals, the two form an effective positive-negative control, directly validating the core theoretical hypothesis of the kurtosis-scale combined weighting mechanism: it only activates the enhancement function for impulse-containing fault signals and suppresses the response to impulse-free pure noise. This further lays a solid theoretical foundation for avoiding false alarms and accurately extracting fault features in subsequent steps, thereby fully demonstrating the theory's validity and reliability.

Figure 1 comprehensively presents the preprocessing chain from the original noisy vibration signal to the generation of a weighted excitation signal. Its core lies in the preliminary enhancement of fault components via dq transformation, fol-

Table 3. Core parameter configuration for experiments.

Parameter Category	Parameter Name	Symbol/Variable	Value
Simulation parameters	Simulation duration	T	2 s
	Total sampling points	N	$\mathrm{int}(T \cdot f_s) = 20480$
	Signal-to-noise ratio	$\mathrm{SNR}_{\mathrm{dB}}$	-5 dB
Duffing system parameters	Damping coefficient	δ	0.5
	Linear stiffness	α	-1.0
	Nonlinear stiffness	β	1.0
	Excitation coefficient	γ	1.0
	Initial state	$y_0, \dot{y}_0$	0.0, 0.0
Kurtosis guidance parameters	Kurtosis threshold	K_{thr}	0.5
	Sigmoid slope	s	10.0
	Sliding window size	$\mathrm{window\_size}$	256
	Kurtosis computation	–	Fisher kurtosis (unbiased)
Fault signal parameters	Fault characteristic frequency	f_{fault}	100 Hz
	Resonance frequency	f_{res}	2000 Hz
	Impulse decay coefficient	ξ	100
	Fault impulse amplitude	A_{fault}	0.5

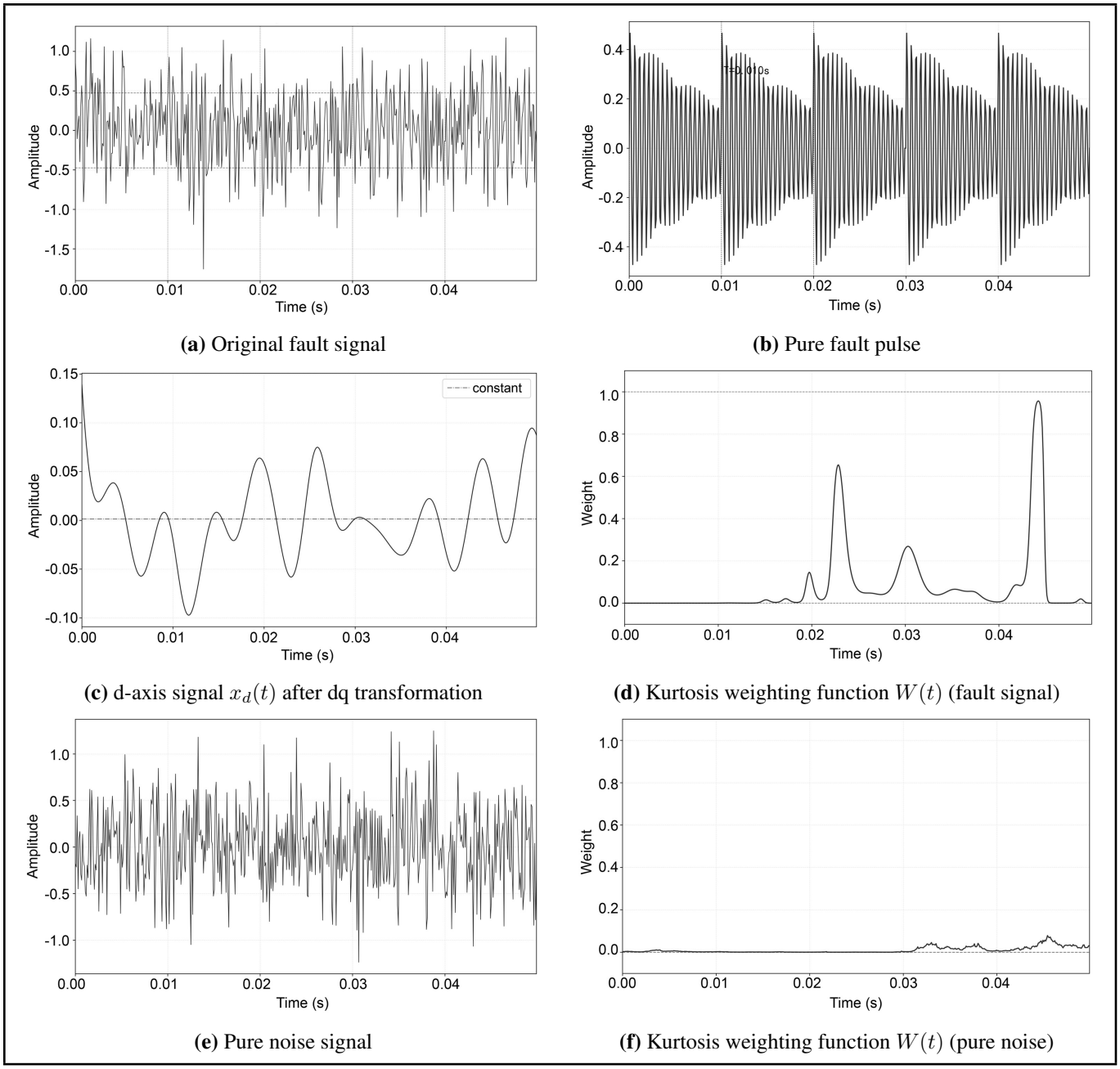

(a) Original fault signal

(b) Pure fault pulse

(c) d-axis signal $x_d(t)$ after dq transformation

(d) Kurtosis weighting function $W(t)$ (fault signal)

(e) Pure noise signal

(f) Kurtosis weighting function $W(t)$ (pure noise)

Figure 1. Signal analysis and preprocessing.

lowed by the construction of an adaptive "intelligent gate" using the combined kurtosis-scale weighting mechanism. The final output is a signal with noise significantly suppressed and fault features precisely focused, establishing the crucial data foundation for subsequent weak-fault detection using the Duffing oscillator.

Validation of synergistic kurtosis guidance and dq transformation is shown in Fig. 2.

Figure 2 compares the dynamic responses of traditional Duffing and the proposed dq–kurtosis Duffing methods under noise-only and fault-excited conditions. Figure 2 consists of four subfigures, intuitively comparing traditional and proposed method performance from signal preprocessing and detection mechanism perspectives.

Figure 2(a) – No dq transformation: Traditional Duffing (pure noise): Under unprocessed pure Gaussian white noise excitation, the traditional Duffing system's phase trajectory exhibits complex, irregular chaotic diffusion in the $(y, \dot{y})$ plane, with large trajectory span. This indicates high noise sensitivity, where random noise pulses induce numerous irregular trajectory mutations of varying amplitudes (pseudo-impulse features), prone to false alarms in fault diagnosis.

Figure 2(b) – No dq transformation: Kurtosis-Duffing (pure noise): Under identical noise excitation, introducing kurtosis guidance fundamentally alters the phase trajectory. Trajectories are strictly confined to a very small region, appearing as uniform, dense, smooth random point clouds. This shows that the kurtosis weighting function $W(t)$ effectively identifies pure noise attributes and substantially suppresses excitation, virtually eliminating noise-induced pseudo-impulse responses and significantly reducing baseline noise and false alarm risk.

Figure 2(c) – With dq transformation: Traditional Duffing (fault signal): After dq transformation preprocessing of the composite signal containing periodic fault impulses and strong noise, input to traditional Duffing yields phase trajectories somewhat narrowed compared to (a), but still diffuse and irregular, with periodic impulse features obscured by residual noise. This indicates that the dq transformation alone is insufficient for feature extraction and that traditional Duffing remains sensitive to residual noise, failing to reveal fault periodicity clearly.

Figure 2(d) – With dq transformation: Kurtosis-Duffing (fault signal): This subfigure demonstrates the complete proposed method (dq transformation + kurtosis-Duffing). The phase trajectory exhibits a clear, regular "limit cycle" structure with periodic, directionally consistent trajectory mutations (sharp peaks) at specific phase points on the cycle. This "ring-peak coupling" topology precisely corresponds to the periodic impulsive fault characteristics. dq transformation successfully extracts fault impulse components, while kurtosis further suppresses residual noise post-transformation; their synergy enables stable excitation of high-SNR dynamical modes synchronized with fault period in the Duffing system.

Figure 2 validates the synergistic role and necessity of the two core components. Horizontal comparisons ((a) vs. (b), (c) vs. (d)) demonstrate the outstanding pseudo-suppression capability of kurtosis guidance in mitigating noise interference. Vertical comparisons ((a) vs. (c), (b) vs. (d)) highlight the critical feature purification role of the dq transformation in creating conditions for subsequent detection. Ultimately, subfigure (d) shows that only combining dq transformation preprocessing with intelligent kurtosis-weighted Duffing detection transforms weak fault impulses into clear, stable, easily identifiable geometric patterns in phase space under strong noise, enabling reliable early fault diagnosis.

6.2. Experimental Analysis

This experiment was conducted on a comprehensive railway bearing fault test rig capable of simulating bearing faults, precise speed control, and multi-dimensional vibration acquisition. It reproducibly simulates typical faults, such as outer race, inner race, and roller damage, providing a standardized environment for validating fault-diagnosis algorithms. The comprehensive railway bearing fault test rig is shown in Fig. 3.

To validate feature extraction capability and speed adaptability of traditional Duffing versus dq-Duffing methods, a high-speed railway bearing AR130-41gP6A with simulated roller damage (outer diameter 240 mm; inner diameter 130 mm; pitch diameter 180.85 mm; roller diameter 26.93 mm; 19 rollers; contact angle 10°) was tested. Operating conditions covered 600 r/min, 900 r/min, and 1200 r/min, corresponding to low-speed (100 km/h), medium-speed (150 km/h), and high-speed (200 km/h) train operation, verifying algorithm adaptability to impulsive fault signals across speeds. The rolling bearing is shown in Fig. 4.

The experiment employed PCB Piezotronics 356A25 triaxial ICP piezoelectric accelerometers (sensitivity 25 mV/g, frequency response 1 Hz to 5000 Hz, measurement range $\pm$ 200 g pk). Per GB/T 6075.2-2011 ("Mechanical vibration—Measurement of vibration on rotating shafts—Part 2: Shaft measurement"), sensors were rigidly mounted via magnetic bases in the vertical (Z) direction on the fault bearing housing, maximizing retention of vibration features from fault impulses while avoiding signal attenuation due to loose installation. The accelerometer test is shown in Fig. 5.

Data acquisition parameters were: sampling frequency 10240 Hz and continuous acquisition duration 10 s per speed condition. The first 1 s transient and last 1 s rundown segments were discarded, retaining the middle 8 s steady-state segment to eliminate non-stationary interference.

Duffing system core parameters were: damping $\delta = 0.5$, linear stiffness $\alpha = -1.0$, and nonlinear stiffness $\beta = 1.0$. The Duffing equation was solved using fourth-order Runge-Kutta with step size 1/10240 (matching sampling frequency). Steady-state displacement-velocity phase trajectories were extracted, and chaotic characteristics were analyzed to quantify fault feature extractability under variable speeds. The experimental algorithm flowchart is shown in Figure 6.

6.2.1. Bearing Fault Phase Diagram Feature Analysis Based on dq-Duffing System

To verify the universality and effectiveness of the proposed dq-Duffing chaotic diagnosis method across speed conditions, roller fault signals (600 r/min, 900 r/min, 1200 r/min) were selected. Phase diagram responses of traditional versus dq-Duffing systems were compared with respect to trajectory morphology, fault discriminability, and diagnostic reliability, re-

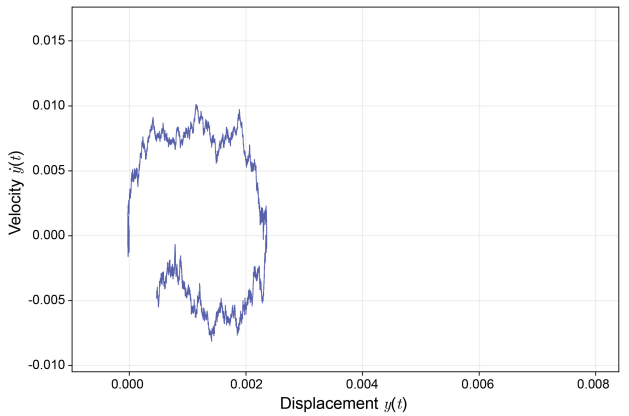

(a) Without dq transformation: Conventional Duffing (pure noise)

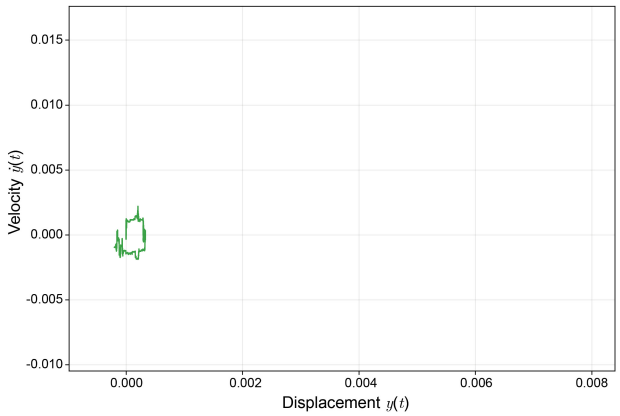

(b) Without dq transformation: Kurtosis-Duffing (pure noise)

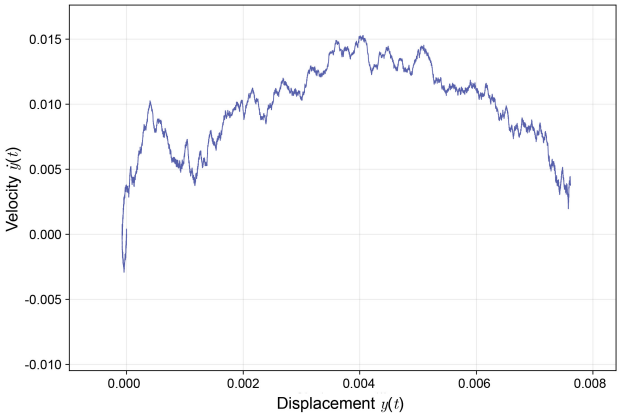

(c) With dq transformation: Conventional Duffing (fault noise)

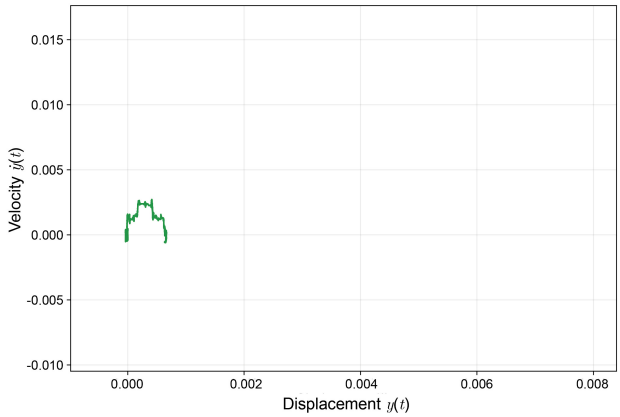

(d) With dq transformation: Kurtosis-Duffing (fault noise)

Figure 2. Experimental comparison figure.

Figure 3. Test rig.

vealing the optimization mechanism of the dq transformation for chaotic diagnosis.

(1) Phase Diagram Feature Analysis at 600 r/min

Figure 7 shows the time-domain waveform of the roller fault signal at 600 r/min, exhibiting superimposed periodic fault impulses and background noise.

Phase diagrams for traditional and dq-Duffing systems are shown in Figs. 8 and 9, respectively.

Figure 8 shows that the traditional Duffing system produces chaotic trajectories without discernible fault patterns:

a) Trajectory morphology: Near-closed chaotic clusters with significant crossing, intense local fluctuations, and indistinct overall boundaries; point cloud diffuse with strong spatial randomness, lacking ordered structure.

b) Fault feature discriminability: Inherent nonlinear fluctuations completely overwhelm periodic impulse energy, preventing effective separation of fault features from chaotic noise; no fault-related information is visible, rendering fault identification ineffective.

Figure 9 demonstrates regular limit-cycle structures with periodic peaks corresponding to fault impulses:

a) Trajectory morphology: After dq transformation preprocessing, trajectories evolve continuously and smoothly without obvious crossing interference, forming a regular composite structure of "closed limit cycle + local impulse clusters"; this arises from the dq transformation's energy focusing, coupling chaotic response with fault features.

b) Fault feature discriminability: Local sharp peaks correspond one-to-one with periodic roller fault impulses, with peak occurrence frequency highly consistent with the calculated fault characteristic frequency; peaks visualize fault

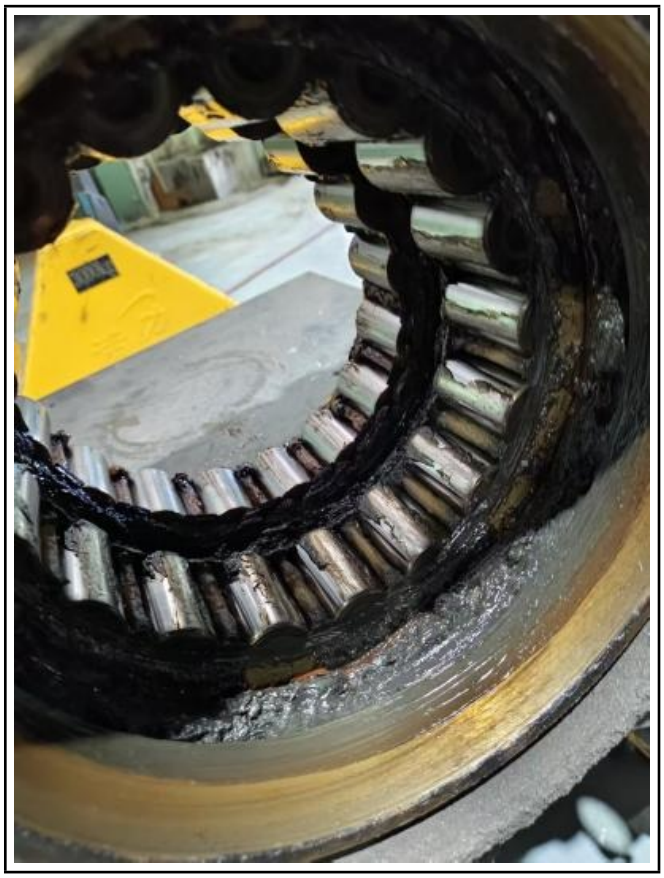

Figure 4. Bearing.

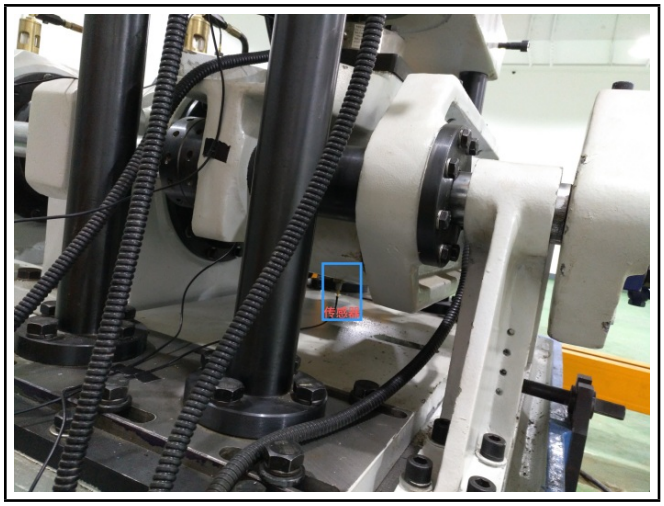

Figure 5. Data acquisition.

impulse energy in chaotic phase space, validating dq transformation enhancement and enabling precise fault feature extraction.

(2) Phase Diagram Feature Analysis at 900 r/min

Figure 10 shows the time-domain waveform at 900 r/min; with increased speed, both impulse frequency and amplitude change, and background noise influence intensifies.

Phase diagrams for traditional and dq-Duffing systems are shown in Figs. 11 and 12.

Figure 11 indicates that traditional Duffing fails to preserve fault features under higher speed and noise:

a) Trajectory morphology: Fragmented random jumps with dispersed, irregular segments lacking a unified evolution outline; chaotic response, disordered, unable to associate trajectories with fault features.

b) Diagnostic effectiveness: Periodic roller impulses smoothed by chaotic fluctuations; fault energy masked by superimposed background and chaotic noise, significantly reducing sensitivity and rendering diagnosis ineffective.

Figure 12 shows stable periodic peak structures synchronized with fault impulses:

a) Trajectory morphology: Unidirectional ordered trend with periodic sharp peaks; good overall continuity without fragmentation; ordered trend stems from dq transformation denoising and energy integration, maintaining trajectory stability.

b) Fault feature discriminability: Sharp peaks exhibit clear periodicity matching the roller fault characteristic period, directly mapping impulses in phase space; even under elevated speed and enhanced noise, dq-Duffing captures fault features precisely, demonstrating strong anti-interference capability.

(3) Phase Diagram Feature Analysis at 1200 r/min

Figure 13 shows the time-domain waveform at 1200 r/min; high speed further increases impulse frequency and signal non-stationarity, posing higher adaptability demands.

Phase diagrams for traditional and dq-Duffing systems are shown in Figs. 14 and 15.

Figure 14 shows chaotic confinement without meaningful fault indication:

a) Trajectory morphology: Confined to narrow phase space with chaotic crossing and random local peaks; response dominated by non-stationarity and high-frequency noise, completely decoupled from fault constraints.

b) Fault feature discriminability: Fault impulse energy fully masked by intense noise and chaotic fluctuations; no identifiable fault-related features, no effective response under high-speed conditions.

Figure 15 confirms robust fault feature extraction over a wide speed range:

a) Trajectory morphology: Regular closed ring structure, continuous and smooth without crossing interference, with clear unified outline; ring formation results from dq transformation's frequency adaptation and energy focusing under high speed, maintaining ordered response.

b) Fault feature discriminability: Periodic sharp peaks on the closed ring strictly match roller fault characteristic frequency, with peak amplitude positively correlated with impulse energy; fault features remain visualizable via peaks even at 1200 r/min, validating wide-speed-range diagnostic universality.

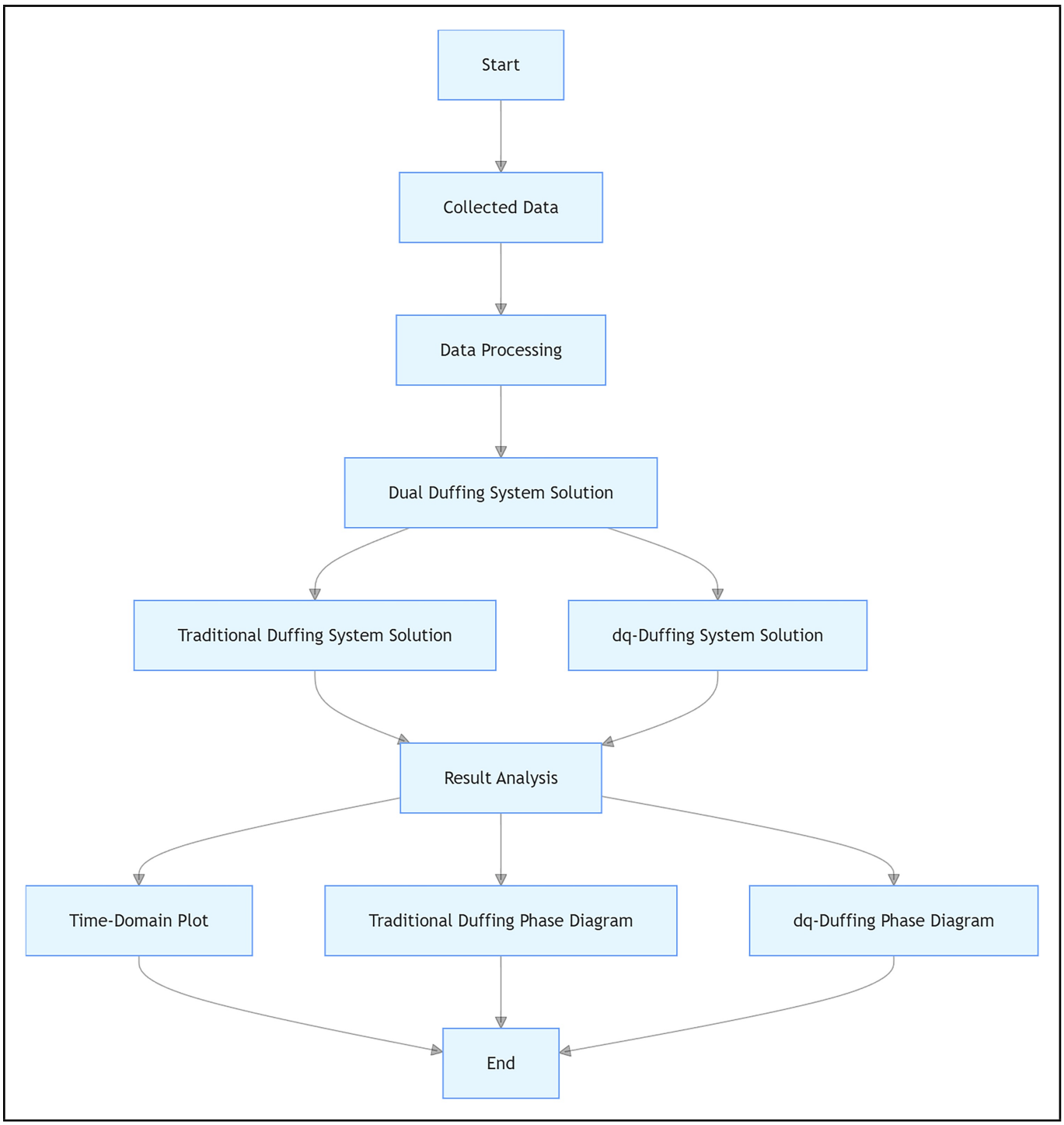

Figure 6. Experimental flowchart.

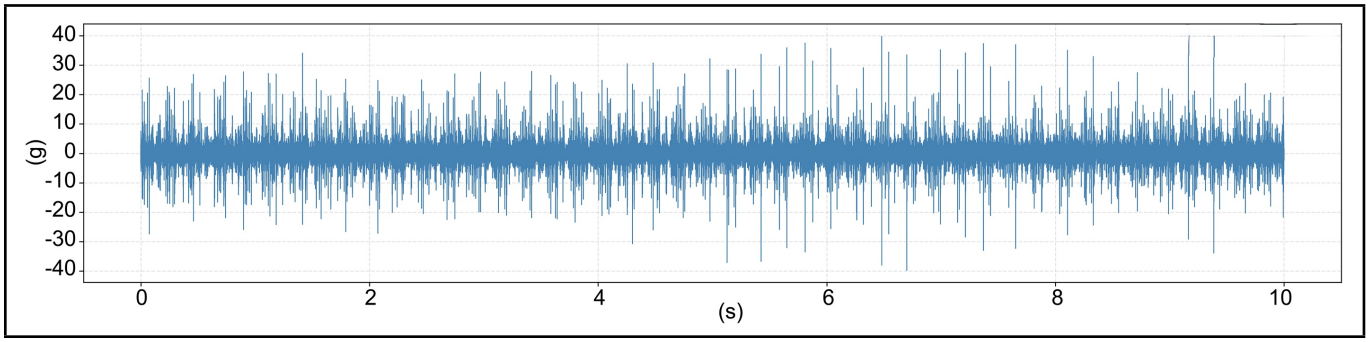

Figure 7. Time-domain waveform.

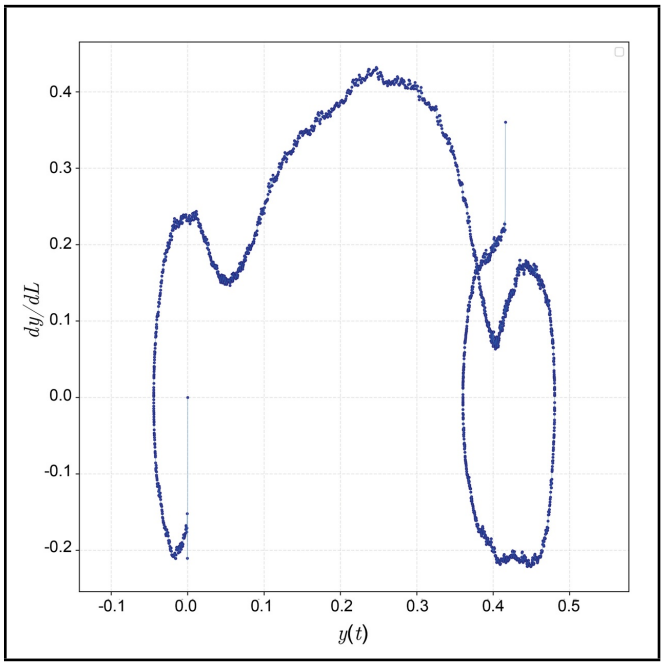

Figure 8. Phase trajectory of traditional duffing system.

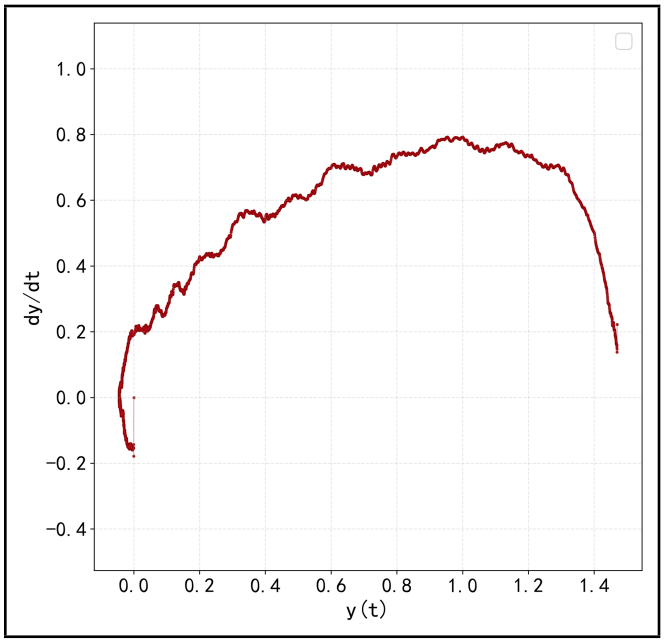

Figure 9. Phase trajectory of dq-duffing system.

(4) Diagnostic Performance Comparison across Speed Conditions

Synthesizing results from the three speed conditions, quantitative comparison of traditional versus dq-Duffing diagnostic performance across trajectory orderliness, fault feature discriminability, and diagnostic reliability is presented in Table 4.

Table 4 compares the performance differences between the traditional Duffing system and the dq-Duffing system under three rotational speeds: 600 r/min (low speed, corresponding to 100 km/h of trains), 900 r/min (medium speed, corresponding to 150 km/h), and 1200 r/min (high speed, corresponding to 200 km/h). The traditional Duffing system is affected by both chaotic noise and signal non-stationarity, resulting in disordered trajectories irrelevant to fault features, with performance deteriorating as speed increases; the dq-Duffing system effectively couples chaotic responses with fault features through the energy focusing and denoising effects of dq transformation, enabling fault feature visualization (ordered trajectories + periodic sharp peaks) over a wide speed range, significantly improving the universality and reliability of chaotic diagnosis.

Traditional Duffing phase responses are influenced by both chaotic noise and signal non-stationarity, yielding disordered trajectories uncorrelated with fault features, and performance deteriorates further at higher speeds. In contrast, dq-Duffing effectively couples chaotic response with fault features via the dq transformation's energy focusing and denoising, consistently visualizing fault features as ordered trajectories + periodic sharp peaks across wide speed ranges, with peak parameters strictly matching the fault characteristic frequency, significantly enhancing universality and reliability of chaotic diagnosis.

6.3. Peak-Ring Coupling Degree

To address essential differences between chaotic or pseudo-closed phase diagrams (chaotic pseudo-rings) and fault impulse rings, a quantitative peak-ring coupling degree (CD) metric is proposed. Its distinguishing feature is the spatiotemporal synchrony between fault-impulse peaks and the ring structure. In contrast, chaotic pseudo-ring peak-like features arise from random noise/speed fluctuations and lack coupling with the ring (Table 5).

Table 5 defines the physical significance of the Peak-Ring Coupling Degree (CD) for distinguishing chaotic/pseudo-closed loop phase diagrams (chaotic pseudo-rings) from fault impulse ring phase diagrams. Peaks in chaotic pseudo-rings originate from random noise or speed fluctuations, with no association with the ring structure; peaks in fault impulse rings originate from periodic bearing fault impulses, concentrated at fixed phases and strongly associated with the ring structure. In the absence of fault peaks, $CD = 0$. By comparing the coupling-degree differences between random-phase peaks (chaos) and synchronous-phase peaks (faults), clear differentiation between faults and chaotic pseudo-features can be achieved, providing a quantitative criterion for fault diagnosis.

6.3.1. Calculation Formula

Peak-ring coupling degree is quantified via normalized polar angle dispersion:

$$CD = 1 - \frac{\sigma_{\theta_{\text{spike}}}}{\pi}; \tag{35}$$

where θ_{spike} is the polar angle of fault impulse peaks in the Duffing phase trajectory; $\sigma_{\theta_{\text{spike}}}$ is the standard deviation of peak polar angles (characterizing peak distribution dispersion on the ring); and π is the maximum polar angle dispersion range, normalizing CD to [0,1]. Higher values approaching 1 indicate greater peak phase concentration and more prominent fault features.

6.3.2. Standardized Calculation Steps

Phase trajectory polar conversion: Extract displacement $y(t)$ and velocity $\dot{y}(t)$ sequences from Duffing solution, converting

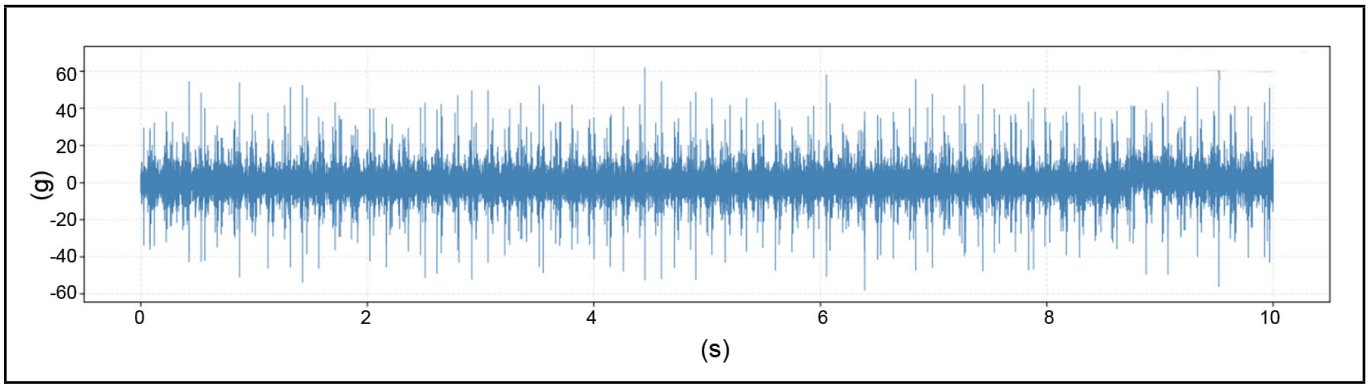

Figure 10. Time-domain waveform.

Table 4. Experimental results across three speed conditions.

Comparison Dimension	Traditional Duffing	dq-Duffing
Trajectory Orderliness	Chaotic fluctuations, no fault feature correspondence	Ordered trajectories + sharp peaks, peaks directly corresponding to roller fault impulses
Fault Feature Discriminability	Fault impulses fully masked by chaos, unrecognizable	Impulse features visualized, directly associable with roller fault period
Diagnostic Reliability	No fault extraction capability	Strong noise resistance, stably presenting fault-associated trajectories

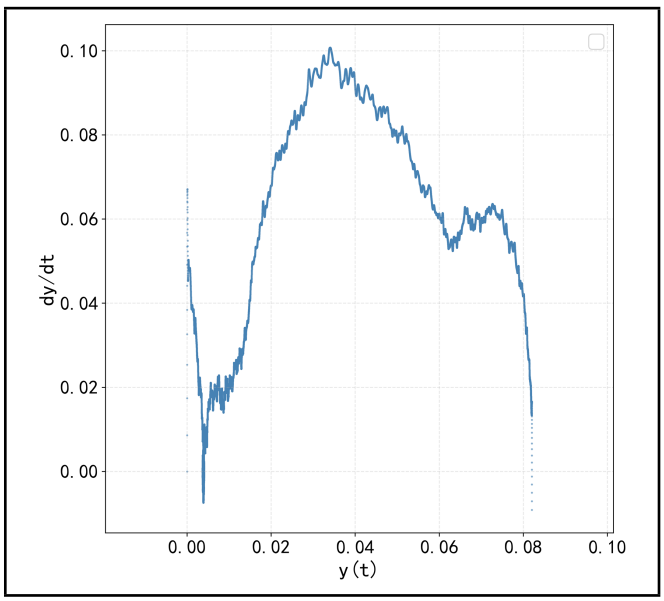

Figure 11. Phase trajectory of traditional duffing system.

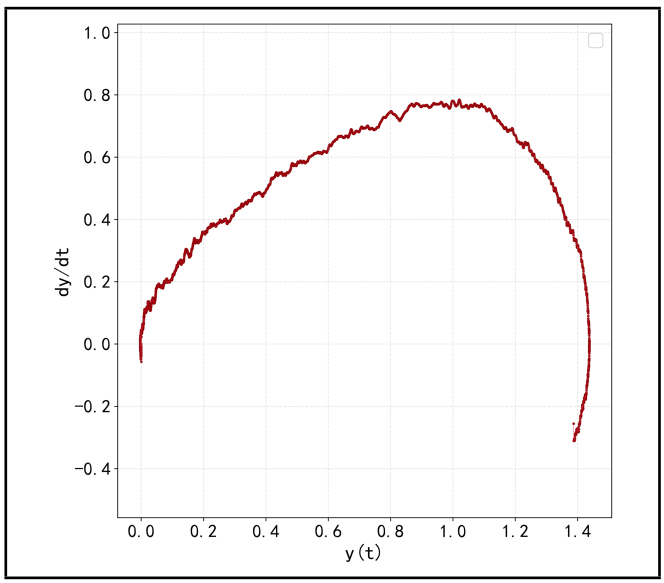

Figure 12. Phase trajectory of dq-duffing system.

to polar coordinates:

$$r = \sqrt{y^2 + \dot{y}^2}, \quad \theta = \arctan 2(\dot{y}, y); \tag{36}$$

where r is the polar radius (characterizing ring radius), and θ is the polar angle (characterizing peak phase position on the ring). The specific calculation of the peak-ring coupling degree can be carried out in the following steps:

1. Effective peak screening: Using 3σ threshold on velocity sequence $\dot{y}(t)$ (σ = standard deviation), extract points exceeding threshold to obtain peak polar angle set θ_{spike}; if no peaks, CD is judged as 0.

2. Dispersion calculation: Compute standard deviation $\sigma_{\theta_{\text{spike}}}$ of θ_{spike}, substitute into core formula ((35)) to obtain CD, with boundary correction ensuring a [0,1] range.

3. Feature decision: $CD \geq m$ is judged as fault impulse ring + peaks, otherwise chaotic (m = fault decision threshold).

6.3.3. Experimental Flowchart and Result Analysis

To clearly present the core execution logic of the experiment, Fig. 16 demonstrates the complete workflow from data preprocessing to fault feature validation.

Core logic of flowchart:

1. Data preprocessing: Steady-state segment extraction, filtering, normalization to eliminate noise and irrelevant components, yielding Duffing-compatible drive signal.

2. Dual Duffing solution: Solve traditional Duffing (enhanced chaos) and dq-Duffing (synchronized fault frequency, weakened chaos) separately, obtaining two phase trajectory sets.

3. Coupling degree calculation: Core steps involve polar angle computation, phase alignment, adaptive peak detection, circular statistics, addressing phase jumps, and noise interference for precise quantification of fault peak phase concentration.

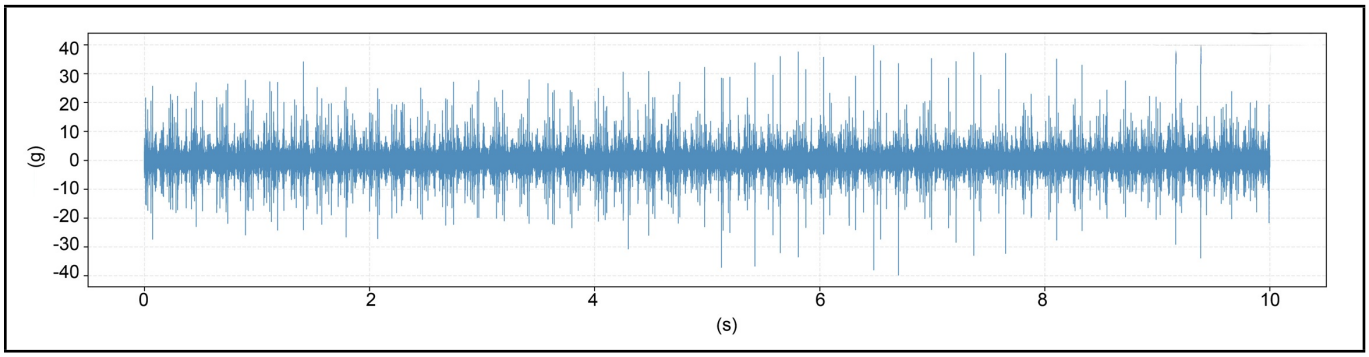

Figure 13. Time-domain waveform.

Table 5. Physical significance of peak-ring coupling degree.

Feature Type	Peak Source	Peak-Ring Coupling Relation	Coupling Degree Range	Physical Significance
Chaotic or pseudo-ring	Random noise /speed fluctuation	No association (random peak distribution)	Determined by data characteristics	No fault features, dominated by chaotic noise
Fault impulse ring + peaks + peaks	Bearing fault periodic impulses	Strong association (peaks concentrated at fixed phases)	Determined by data characteristics	Fault impulses drive ring structure, features prominent

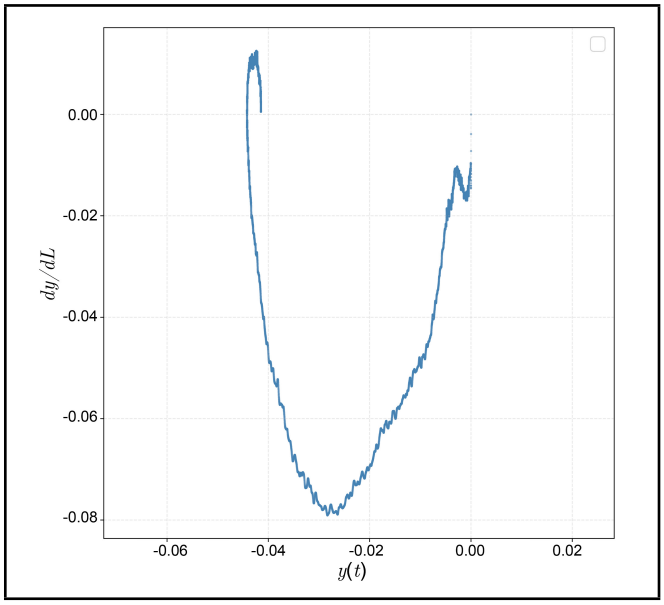

Figure 14. Phase trajectory of traditional duffing system.

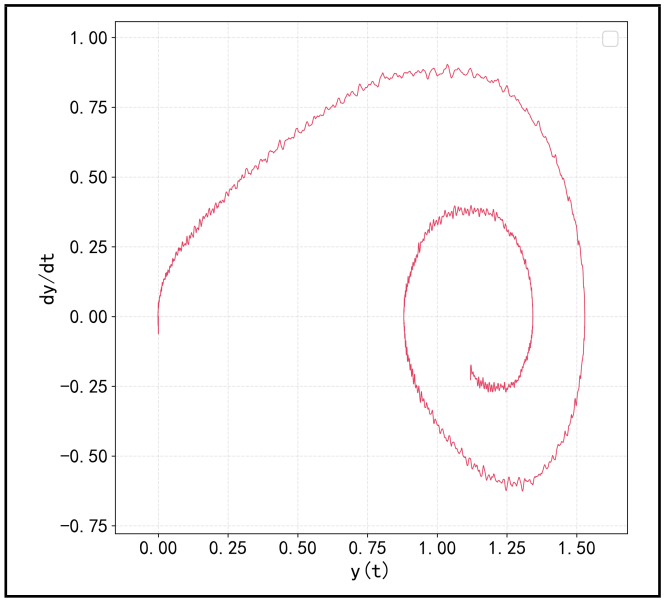

Figure 15. Phase trajectory of dq-duffing system.

4. Result analysis: Compare coupling degree and strong peak counts to validate the dq-Duffing fault feature extraction superiority.

Coupling degree comparison between traditional and dq-Duffing is shown in Fig. 17. Figure 17 compares coupling degree values, demonstrating the superiority of the proposed method:

1. dq-Duffing exhibits significantly superior fault feature extraction: Across all groups, dq-Duffing CD exceeds traditional Duffing, validating the dq transformation's role in suppressing Duffing chaos and enhancing peak-ring coupling feature extraction.

2. Group 2 shows most typical discrimination: Traditional Duffing CD only 0.0845 (near chaotic), while dq-Duffing reaches 0.6116 (near fault threshold), highlighting strong discrimination between chaotic pseudo-ring and fault ring + peaks under this condition.

3. Group 3 exhibits most prominent fault features: dq-Duffing CD reaches 0.8852, indicating extremely strong phase concentration of fault impulse-ring, with dq-Duffing fully locking onto fault features.

6.4. Comparative Analysis

This section processes fault signals using wavelet transforms, stochastic resonance, and a dq-Duffing chaotic oscillator, comparing time-domain waveforms and frequency-domain spectral features; peak SNR at the fault frequency and its harmonics is quantitatively assessed to validate the dq-Duffing's effectiveness and superiority in extracting bearing fault features under strong noise.

Raw signal is shown in Fig. 18. Figure 18 shows that both time-domain and frequency-domain representations fail under low SNR.

Raw signal time-domain (Figure 18(a)): Blue waveform shows raw vibration time variation, severely contaminated by strong noise; 120 Hz periodic fault signal present but completely submerged in the time domain.

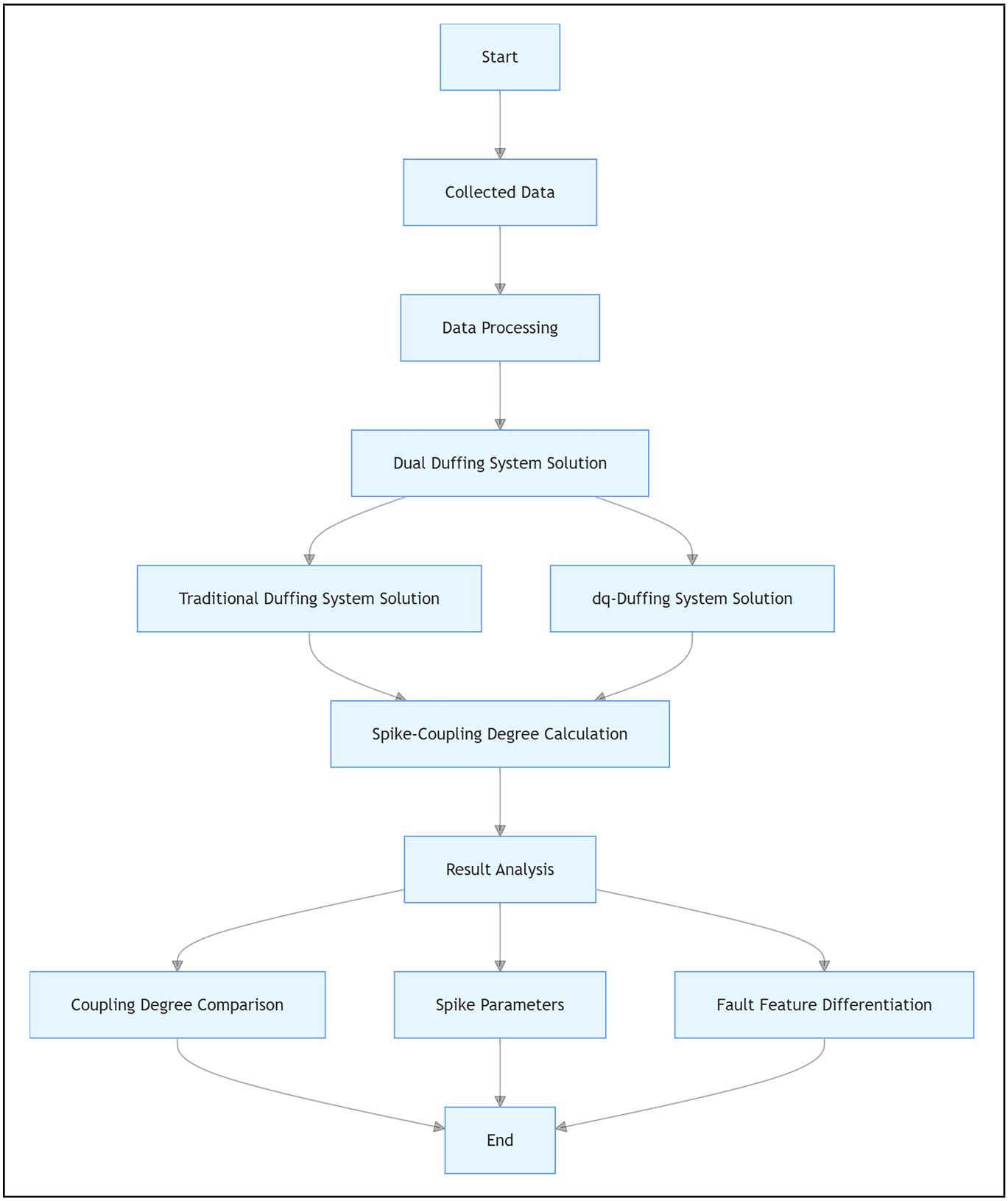

Figure 16. Experimental flowchart.

Raw signal spectrum (Figure 18(b)): Green curve shows frequency distribution, with red dashed lines marking 120 Hz (fundamental) and 240 Hz (second harmonic); spectral peaks exist but are inconspicuous, comparable to the background noise level, rendering conventional spectral analysis ineffective due to extremely low SNR.

Wavelet transform results are shown in Fig. 19. Figure 19 shows partial enhancement of fault-related components.

Wavelet transform output time-domain (Figure 19(c)): As a time-frequency method analyzing signal with multi-scale wavelets, noise is somewhat suppressed compared to the raw signal, and the waveform is smoother with some periodic traces visible but still unclear.

Wavelet transform spectrum (Figure 19(d)): Relatively prominent peaks appear at 120 Hz and 240 Hz, effectively suppressing some noise and enhancing fault frequency detectabil-

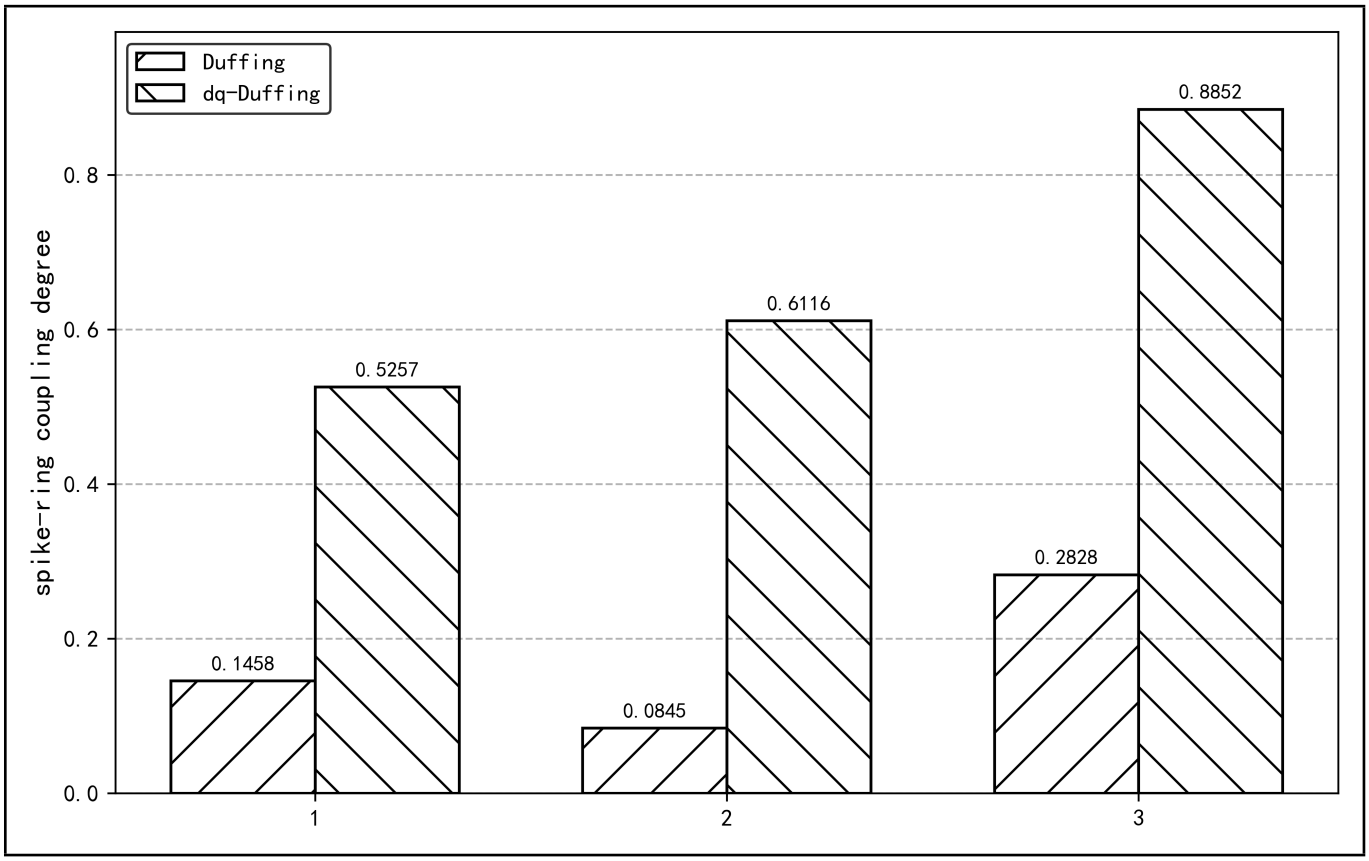

Figure 17. Coupling degree comparison.

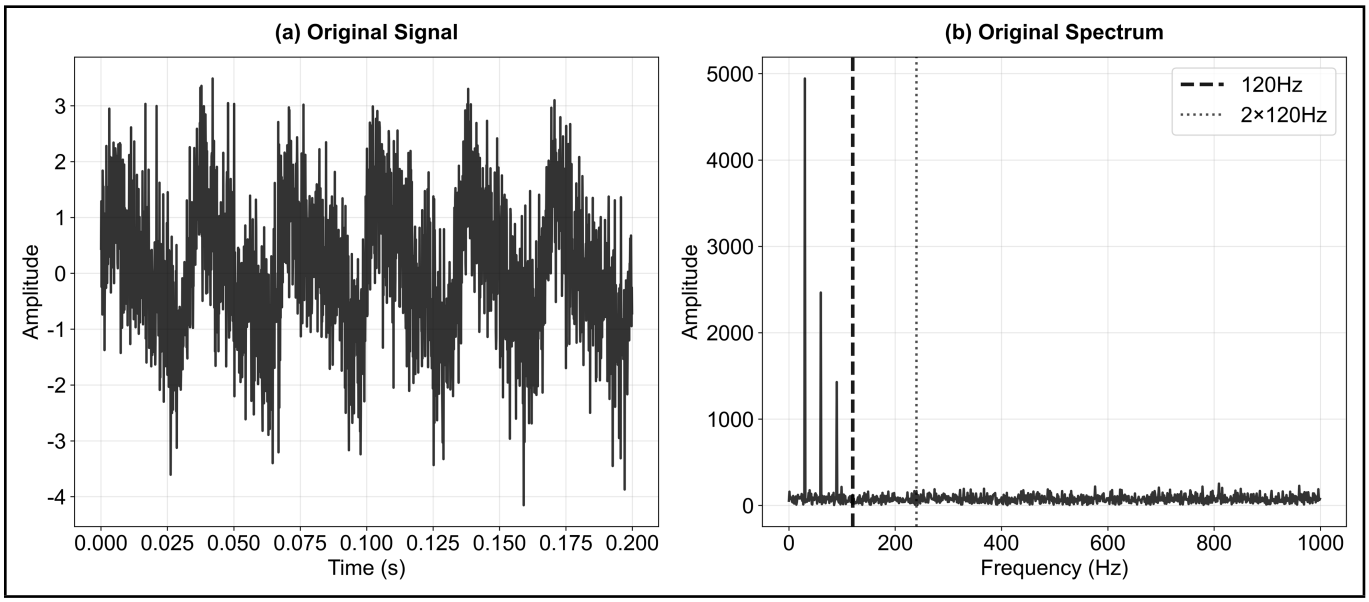

Figure 18. Raw signal.

ity, though performance is limited under low SNR.

Stochastic resonance results are shown in Fig. 20. Figure 20 indicates limited fault extraction capability under extremely low SNR.

Stochastic resonance output time-domain (Figure 20(e)): Leveraging a nonlinear system where noise energy enhances weak signals under specific parameters, the yellow waveform shows some regularity, but periodic features remain indistinct.

Stochastic resonance spectrum (Figure 20(f)): Weak response only near 240 Hz (second harmonic), almost no detection at 120 Hz fundamental. Detection of fundamental weak signals under low SNR, highly sensitive to SNR, and parameter tuning.

dq-Duffing results are shown in Fig. 21. Figure 21 confirms that dq-Duffing simultaneously reveals fault impulses in phase space and frequency domain.

Duffing phase diagram (Figure 21(g)): Purple trajectory shows Duffing oscillator phase-space motion (x-axis displacement, y-axis velocity), exhibiting a complex yet structured pattern; the system transitions from chaos to regular motion when the input contains specific frequency components.

dq transformation components (Figure 21(h)): Red and blue

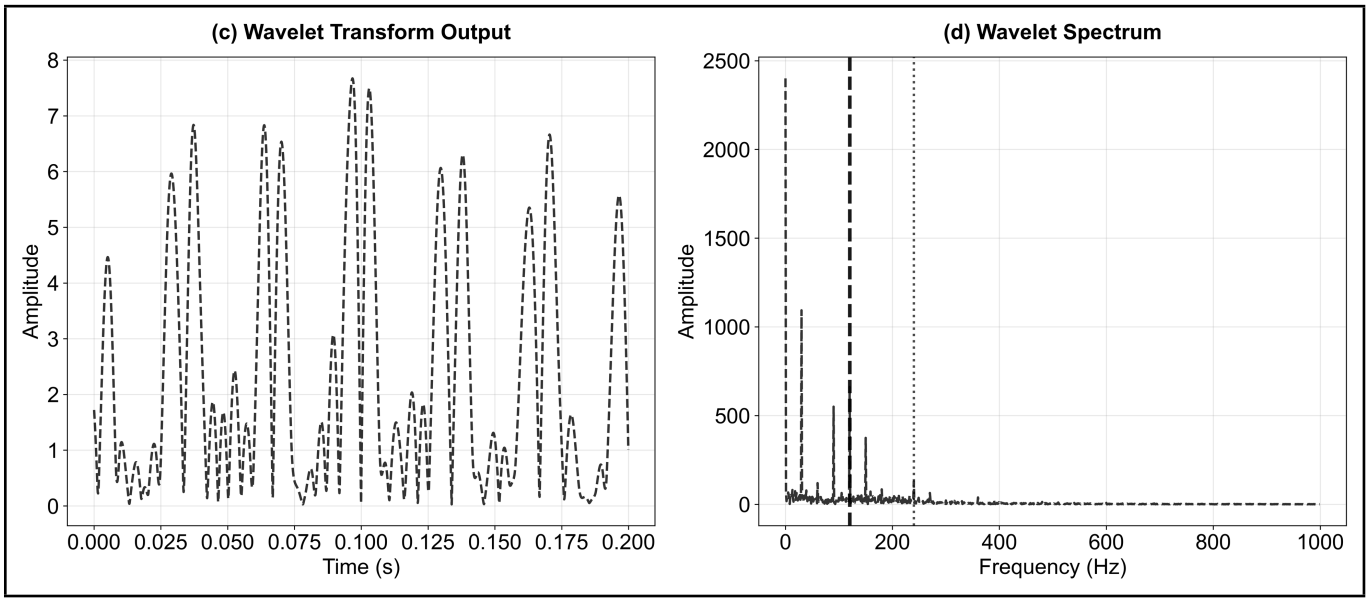

Figure 19. Wavelet analysis plot.

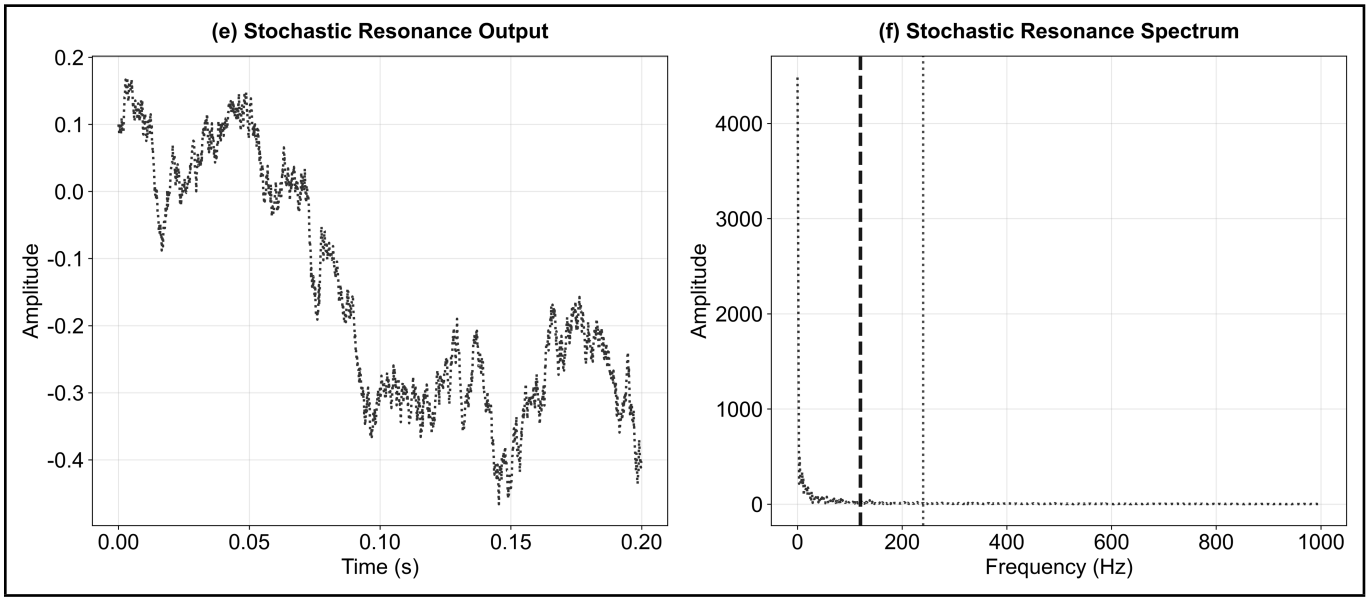

Figure 20. SR analysis plot.

curves represent orthogonal components post-dq transformation; dq transforms time-domain impulses into "DC" or low-frequency signals in the rotating frame, both showing clear periodicity.

dq-Duffing spectrum (Figure 21(i)): Red spectrum clearly displays 120 Hz fundamental and harmonics; peaks at 120 Hz, 240 Hz, 360 Hz, 480 Hz, etc. are weakly visible but present, capable of clearly extracting complete harmonic structure under low SNR.

A summary comparison of the three methods is presented in Table 6.

Table 6 compares the performance of three methods (Wavelet Transform, Stochastic Resonance, and dq-Duffing) for bearing fault detection under low-SNR conditions. As a traditional time-frequency method, Wavelet Transform achieves moderate noise suppression and feature extraction; Stochastic Resonance can theoretically utilize noise energy but is practically parameter-sensitive with poor fundamental frequency detection; the dq-Duffing method combines the anti-noise capability of chaotic systems with the frequency selectivity of dq transformation, enabling extraction of complete harmonic structures even at extremely low SNR with high diagnostic certainty, making it particularly suitable for detecting weak periodic impulse faults in bearings.

7. CONCLUSION

1. **Research background and core problem**

   Periodic impulsive fault signals in electric locomotive bearings are readily overwhelmed by strong noise. Early fault features are weak and exhibit extremely low energy, leading traditional time/frequency-domain analysis and signal decomposition methods to suffer from feature distortion, mode mixing, and parameter sensitivity under low SNR, hindering precise diagnosis. While single Duffing chaotic systems are sensitive to weak periodic signals, they lack multi-component separation capability and exhibit noise tolerance that is heavily influenced by param-

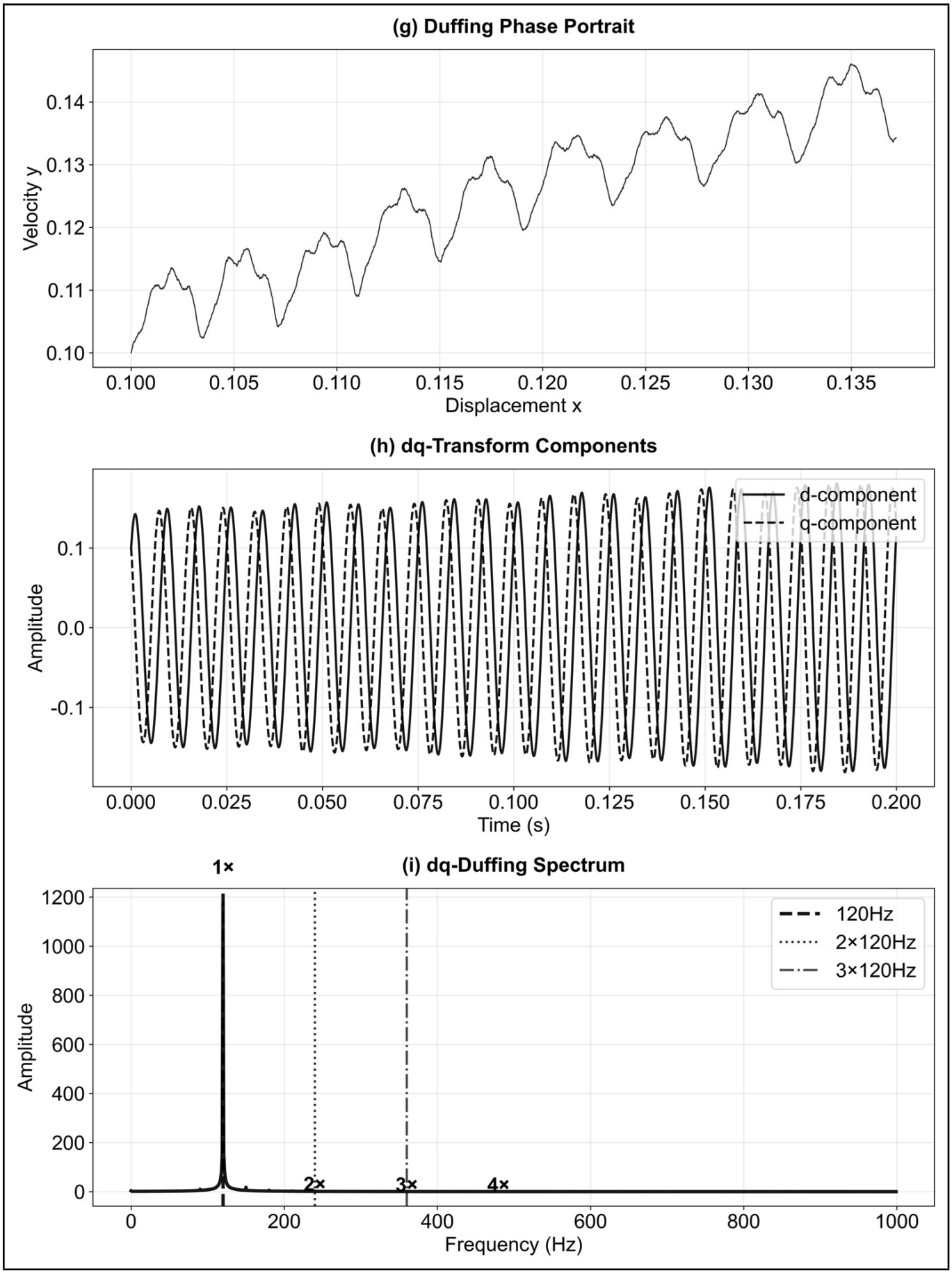

Figure 21. dq-duffing analysis plot.

Table 6. Characteristic comparison of three fault detection methods.

Characteristic Comparison	Wavelet Transform	Stochastic Resonance	dq-Duffing
Detection Principle	Time-frequency decomposition, multi-resolution analysis	Nonlinear system, noise-assisted enhancement	Chaotic system + coordinate transformation
120 Hz Detection	Medium-strength peaks	Almost none	Clear sharp peaks
Harmonic Structure	Relatively complete multi-order harmonics	Weak response only at second harmonic	Complete multi-order harmonics
Noise Suppression	Partial suppression	Limited effect	Significant suppression
Diagnostic Certainty	Medium, single-frequency evidence	Low, indistinct response	High, harmonic fingerprint confirmation
Real-time Performance	Moderate computation	Parameter-sensitive, requires tuning	Higher computation but stable
Applicable Scenarios	General SNR conditions	Specific-parameter weak signals	Extremely low SNR impulsive faults

eters, failing to meet engineering demands for the full pipeline of signal separation, noise suppression, and weak feature enhancement.

2. **Core method framework and theoretical support**

A bearing fault detection method integrating dq transformation, kurtosis statistics, and Duffing chaotic system is proposed, constructing a progressive separation suppression enhancement framework with theoretical support throughout:

dq transformation separation mechanism: Using virtual two-phase technology, the Hilbert transform constructs orthogonal signals forming an α-β frame, followed by rotation synchronized with the fault characteristic frequency to convert single-channel periodic impulses into slowly varying d-axis signals, decoupling fault features from interference and providing higher-SNR input.

Kurtosis adaptive suppression mechanism: Exploiting statistical difference between fault impulses (non-Gaussian, high kurtosis) and noise (Gaussian, low kurtosis), sliding-window Fisher kurtosis constructs a sigmoid gating function to dynamically regulate excitation intensity, with a weight near 0 during noise dominance to suppress pseudo-impulses, near 1 during fault impulses to preserve features, raising pseudo-response threshold from a dynamics perspective.

Duffing system enhancement mechanism: Optimizing constant-biased bistable Duffing parameters, DC bias tilts potential wells to reduce inter-well energy demand for weak signals, balancing sensitivity and stability; the system produces ring-peak coupling phase trajectories for purified fault signals, transforming weak features into identifiable topological structures. Phase trajectory analysis under four excitations (pure noise, constant, constant+noise, constant+noise+impulses) validates effectiveness.

Quantitative decision theory: Proposed peak-ring coupling degree metric quantifies spatiotemporal synchrony between fault peaks and ring via normalized polar angle dispersion, enabling unambiguous fault versus chaotic pseudo-feature discrimination.

3. **Key innovations**

Proposed adaptive fusion strategy for dq transformation and kurtosis statistics, transforming kurtosis from an offline metric to an online control parameter for selective fault impulse response.

Constructed closed-loop separation suppression enhancement quantification framework, resolving traditional Duffing noise interference while overcoming limitations of single signal processing techniques.

Optimized Duffing DC bias parameters and phase trajectory quantification, enhancing diagnostic robustness and certainty under low SNR and wide speed ranges.

4. **Method advantages**

The method achieves evolution from indiscriminate sensitivity to selective acuity, with core advantages in three aspects: strong noise suppression via synergistic kurtosis gating and dq transformation, effectively filtering Gaussian noise and pseudo-impulses; precise feature extraction, with Duffing transforming weak impulses into stable ring-peak coupling trajectories with complete harmonics; broad operating condition adaptability, stably outputting diagnostic results across low SNR and wide speeds with low false alarms and high reliability, providing an effective technical means for early fault diagnosis of electric locomotive bearings.

5. **Core experimental validation results**

Simulation and real-machine experiments confirm the method's effectiveness: Under low-SNR simulation, phase trajectories exhibit clear ring-peak coupling with prominent fault frequency and harmonics. Real-machine experiments spanning 600-1200 r/min show ordered trajectories with peaks strictly matching fault frequency, unlike disordered traditional Duffing trajectories. Compared with wavelet transform (moderate extraction) and stochastic resonance (parameter-sensitive, weak fundamental detection), the proposed method exhibits superior noise suppression, complete harmonics, higher diagnostic reliability, and anti-interference capability; peak-ring coupling degree quantification further validates the superiority of fault feature extraction.

6. **Future outlook**

Future work may optimize frequency-adaptive dq transformation algorithms, explore integration with deep learning models to reduce manual parameter tuning, and improve generalization under complex conditions. This can also enhance computational efficiency to facilitate real-time online monitoring in engineering applications.

REFERENCES

[1] Zang, Y., Wei, S. G., Cai, B. G. et al. Methods for fault diagnosis of high-speed railways: a review, *Proceedings of the Institution of Mechanical Engineers, Part O: Journal of Risk and Reliability*, **233**(5), 908–922, (2019). https://doi.org/10.1177/1748006X18823932

[2] Zhong, Z. B. L. and Huang, R. *Mechanical Fault Diagnosis*, China Machine Press, Beijing, (2002).

[3] Huang, N. E., Shen, Z., Long, S. R. et al. The empirical mode decomposition and the Hilbert spectrum for nonlinear and non-stationary time series analysis, *Proceedings of the Royal Society A: Mathematical, Physical and Engineering Sciences*, **454**, 903–955, (1998). https://doi.org/10.1098/rspa.1998.0193

[4] Chen, K., Li, F. C., and Li, H. G. Fast adaptive empirical mode decomposition method and its application to bearing fault diagnosis, *Journal of Vibration, Test and Diagnosis*, **36**(4), 647–652, (2016). https://doi.org/10.16450/j.cnki.issn.1004-6801.2016.04.009

[5] Xue, Q., Tian, R. L., Li, H. P. et al. Period identification method of variance curve for harmonic weak signal features, *Journal of Vibration, Test and Diagnosis*, **45**(1), 51–56, (2025). https://doi.org/10.16450/j.cnki.issn.1004-6801.2025.01.008

[6] Zhang, L., Ji, Y. D., and Luo, M. K. Parameter estimation of weak signal based on the steady attractor of Duffing oscillator, *Chinese Journal of Electronics*, **28**(4), 781–788, (2019). https://doi.org/10.1049/cje.2019.05.005

[7] Gokyildirim, A., Uyaroglu, Y., Pehlivan, I. et al. A novel chaotic attractor and its weak signal detection application, *Optik – International Journal for Light and Electron Optics*, **127**(19), 7889–7895, (2016). https://doi.org/10.1016/j.ijleo.2016.05.150

[8] Li, G. Z., Ta, N. L., and Li, X. Weak signal detection method based on the coupled Lorenz system and its application in rolling bearing fault diagnosis, *Applied Sciences*, **10**(12), 4086, (2020). https://doi.org/10.1049/iet-spr.2020.0203.

[9] Mahmut, A., Nazmi, Y., and Gediz Akdeniz, K. Automated system for weak periodic signal detection based on Duffing oscillator, *IET Signal Processing*, **14**(10), 710–716, (2020). https://doi.org/10.1049/iet-spr.2020.0203

[10] Lai, Z. H., Leng, Y. G., Sun, J. Q. et al. Research on variable scale weak feature signal detection method based on Duffing oscillator, *Acta Physica Sinica*, **61**(5), 60–68, (2012). https://doi.org/10.7498/aps.61.050502

[11] Tian, R. L., Zhao, Z .J., and Xu, Y. Variable scale-convex-peak method for weak signal detection, *Science China Technological Sciences*, **64**(2), 331–340, (2021). https://doi.org/10.1007/s11431-019-1530-4

[12] Zheng, K., Li, T. A., Su, Z. Q. et al. Sparse elitist group lasso denoising in frequency domain for bearing fault diagnosis, *IEEE Transactions on Industrial Informatics*, **17**(7), 4681–4691, (2021). https://doi.org/10.1109/TII.2020.3011065

[13] Zhang, D. and Lu, G. L. Fault diagnosis of rolling bearings based on graph modeling feature extraction, *Journal of Vibration, Test and Diagnosis*, **41**(2), 249–253, (2021).

[14] Coccolo, M. and Sanjuán, M. A. F. Transmitted resonance in a coupled system, *Communications in Nonlinear Science and Numerical Simulation*, **135**, 108068, (2024). https://doi.org/10.1016/j.cnsns.2024.108068

[15] Coccolo, M., Litak, G., Seoane, J. M. et al. Energy Harvesting Enhancement by Vibrational Resonance, *International Journal of Bifurcation and Chaos*, **24**(06), 1430019, (2014). https://doi.org/10.1142/S0218127414300195

[16] Cantisán, J., Coccolo, M., Seoane, J. M. et al. Delay-Induced Resonance in the Time-Delayed Duffing Oscillator, *International Journal of Bifurcation and Chaos*, **30**(03), 2030007, (2020). https://doi.org/10.1142/S0218127420300074

[17] Coccolo, M., Zhu, B. B., Sanjuán, M. A. F. et al. Bogdanov-Takens resonance in time-delayed systems, *Nonlinear Dynamics*, **91**, 1939–1947, (2018). https://doi.org/10.1007/s11071-017-3992-1

[18] Coccolo, M., Seoane, J. M., and Sanjuán, M. A. F. Fractional damping induces resonant behavior in the Duffing oscillator, *Communications in Nonlinear Science and Numerical Simulation*, **133**, 107965, (2024). https://doi.org/10.1016/j.cnsns.2024.107965

[19] Roy, S., Coccolo, M., and Sanjuán, M. A. F. Parametric autoresonance with time-delayed control, *Physical Review E*, **111**(01), 014225, (2025). https://doi.org/10.1103/PhysRevE.111.014225

[20] Wang, Q. B., Zhang, X., and Yang, Y. J. Dynamic behaviors analysis of asymmetric stochastic delay differential equations with noise and application to weak signal detection, *Symmetry*, **11**(11), 1428, (2019). https://doi.org/10.3390/sym11111428

[21] Simiu, E. and Frey, M. Melnikov processes and noise-induced exits from a well, *Journal of Engineering Mechanics*, **122**(3), 263–270, (1996). https://doi.org/10.1061/(ASCE)0733-9399(1996)122:3(263)

[22] Frey, M. and Simiu, E. Noise-induced chaos and phase space flux, *Physica D: Nonlinear Phenomena*, **63**(3/4), 321–340, (1993). https://doi.org/10.1016/0167-2789(93)90114-G

[23] Yagasaki, K. Melnikov processes and chaos in randomly perturbed dynamical systems, *Nonlinearity*, **31**, 3057–3085, (2018). https://doi.org/10.1088/1361-6544/aab89f